J. Fluid Mech. (2020), *vol.* 882, A26. © Cambridge University Press 2019
doi:10.1017/jfm.2019.835

Data-driven decomposition of the streamwise turbulence kinetic energy in boundary layers. Part 2. Integrated energy and A_1

Woutijn J. Baars[1,†] **and Ivan Marusic**[2]

[1]Department of Engineering, Aarhus University, 8000 Aarhus C, Denmark

[2]Department of Mechanical Engineering, The University of Melbourne, VIC 3010, Australia

(Received 6 October 2018; revised 31 July 2019; accepted 13 October 2019)

Scalings of the streamwise velocity energy spectra in turbulent boundary layers were considered in Part 1 (Baars & Marusic, *J. Fluid Mech.*, vol. 882, 2020, A25). A spectral decomposition analysis provided a means to separate out attached and non-attached eddy contributions and was used to generate three spectral sub-components, one of which is a close representation of the spectral signature induced by self-similar, wall-attached turbulence. Since sub-components of the streamwise turbulence intensity $\overline{u^2}$ follow from an integration of the velocity energy spectra, we here focus on the scaling of the former. Wall-normal profiles and Reynolds-number trends of the three individual, additive sub-components of the streamwise turbulence intensity are examined. Based on universal trends across all Reynolds numbers considered, some evidence is given for a Townsend–Perry constant of $A_1 = 0.98$, which would describe the wall-normal logarithmic decay of the turbulence intensity per Townsend's attached-eddy hypothesis. It is also demonstrated how this constant can be consistent with the Reynolds-number increase of the streamwise turbulence intensity in the near-wall region.

Key words: turbulent boundary layers, boundary layer structure

1. Introduction and context

Wall-normal trends of the streamwise turbulence intensity (TI), denoted as $\overline{u^2}$, are a prerequisite to modelling efforts of wall-bounded turbulence. Several models for $\overline{u^2}$ are hypothesis based. For instance, the model of Marusic & Kunkel (2003) was inspired by the attached-eddy hypothesis (AEH, Townsend 1976), while Monkewitz & Nagib (2015) constructed a model via asymptotic expansions and Chen, Hussain & She (2018) via a dilation symmetry approach. The works of Vassilicos *et al.* (2015) and Laval *et al.* (2017) derived a model for the streamwise TI by introducing a new spectral scaling at the very large-scale end of the spectrum, beyond the scales associated with a k_x^{-1} region, where k_x is the streamwise wavenumber. All models require validation and calibration for the streamwise TI (Monkewitz, Nagib & Boulanger 2017) and assumptions are inevitable for extrapolated conditions. More

† Email address for correspondence: baars@eng.au.dk

importantly, validation of the underlying spectra is often avoided, which could result in questioning of the model assumptions. Even with available wall-normal profiles of $\overline{u^2}$ and its spectral distribution, from both numerical computations and experiments (e.g. Marusic, Mathis & Hutchins 2010*a*), definitive scalings remain elusive and continue to be of research interest. The difficulty in finding empirical scaling trends is mainly due to the weak dependence of $\overline{u^2}$ on the Reynolds number, the limited Reynolds-number range over which direct numerical simulations are feasible/available and the practical challenges associated with experimental acquisition of fully resolved data.

Velocity energy spectra give information on how the streamwise TI is distributed across wavenumbers, because the streamwise TI (the velocity variance or normal stress) equates to the integrated spectral energy via Parseval's theorem (e.g. $\overline{u^2} = \int \phi_{uu}\,\mathrm{d}k_x$, where ϕ_{uu} is the streamwise velocity spectrum). Part 1 (Baars & Marusic 2020) considered the streamwise velocity energy spectra – and in particular by way of a spectral decomposition to separate out several wall-attached and non-attached eddy contributions – thus allowing an evaluation of the wall-normal profiles and Reynolds-number trends of three individual, additive sub-components of the streamwise TI.

First, this introduction addresses the widely researched logarithmic decay of the streamwise TI within the outer region of turbulent boundary layers (TBLs) in § 1.1. Then, we discuss the contentious issue of the k_x^{-1} scaling in the streamwise velocity spectrum $\phi_{uu}(k_x)$, where k_x is the streamwise wavenumber (and $\lambda_x \equiv 2\pi/k_x$ is the streamwise wavelength). We briefly review Part 1 in § 1.2, which presented a data-driven spectral decomposition.

Notation in this paper is identical to that used in Part 1. Coordinates x, y and z denote the streamwise, spanwise and wall-normal directions of the flow, whereas the friction Reynolds number $Re_\tau \equiv \delta U_\tau/\nu$ is the ratio of δ (the boundary layer thickness) to the viscous length scale ν/U_τ. Here ν is the kinematic viscosity and $U_\tau = \sqrt{\tau_o/\rho}$ is the friction velocity, with τ_0 and ρ being the wall-shear stress and fluid density, respectively. When a dimension of length is presented in outer-scaling, it is normalized with scale δ, while a viscous-scaling with ν/U_τ is signified with superscript '+'. Lower-case u represents the Reynolds decomposed fluctuations and U the absolute mean.

1.1. *Townsend–Perry constant A_1 in the context of the turbulence intensity and spectra*

Townsend (1976) hypothesized that the energy-containing motions in TBLs are comprised of a hierarchy of geometrically self-similar eddying motions, that are inertially dominated (inviscid), attached to the wall and scalable with their distance from the wall (Marusic & Monty 2019). According to the classical model of attached eddies (Perry & Chong 1982), the wall-normal extents of the smallest attached eddies scale with inner variables, e.g. $100\nu/U_\tau$, while the largest scale with δ. Consequently, Re_τ is a direct measure of the attached-eddy range of scales. Following the attached-eddy modelling framework, the streamwise TI within the logarithmic region adheres to

$$\overline{u^2}^+ = B_1 - A_1 \ln\left(\frac{z}{\delta}\right), \tag{1.1}$$

where A_1 and B_1 are constants; A_1 was dubbed the Townsend–Perry constant. A scaling of $\phi_{uu} \propto k_x^{-1}$ (or a plateau in the premultiplied spectrum $k_x^+\phi_{uu}^+$) is consistent

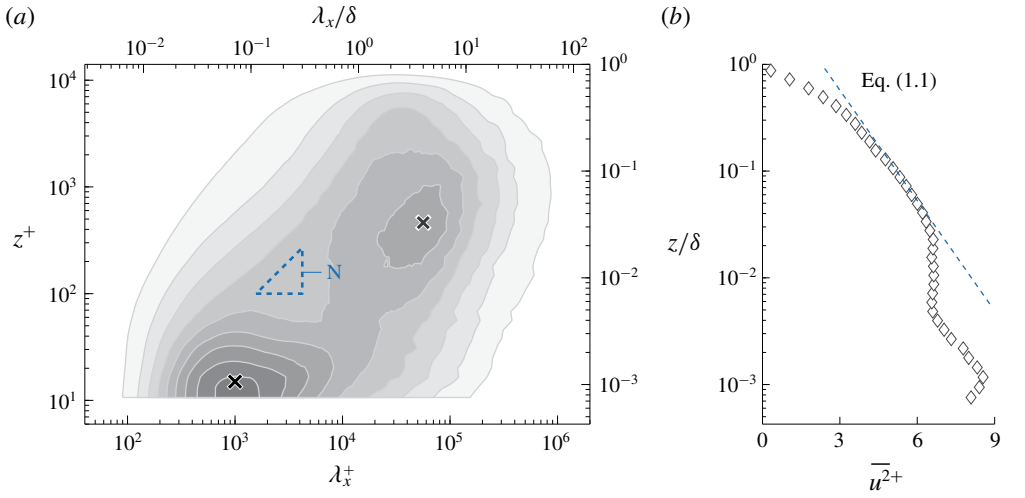

FIGURE 1. (*a*) Premultiplied energy spectrogram $k_x^+\phi_{uu}^+$ (filled iso-contours 0.2 : 0.2 : 1.8) at $Re_\tau \approx 14\,100$ (Baars, Hutchins & Marusic 2017*a*). Triangle 'N' refers to the k_x^{-1} region identified by Nickels *et al.* (2005). (*b*) Turbulence intensity profile and (1.1) with $A_1 = 1.26$ and $B_1 = 2.30$.

with the presence of a sufficient range of attached-eddy scales. Such a spectral scaling for the energy-containing, inertial range of anisotropic scales can be predicted with the aid of dimensional analysis, a spectral overlap argument and an assumed type of eddy similarity (e.g. Perry & Abell 1975; Davidson & Krogstad 2009). Perry, Henbest & Chong (1986) related the plateau magnitude of the premultiplied spectrum back to (1.1), resulting in

$$k_x^+\phi_{uu}^+ = A_1. \tag{1.2}$$

An underlying assumption of (1.1), in combination with (1.2), is that all energy is induced by self-similar attached-eddy motions. And so, from detailed studies on the streamwise turbulence kinetic energy, from which profiles of $\overline{u^2}(z)$ and streamwise spectra ϕ_{uu} are available, the Townsend–Perry constant A_1 inferred via either (1.1) or (1.2) must be equal, of course provided that attached-eddy turbulence dictates the scaling.

Thus far, evidence for (1.2) has been inconclusive, mainly due to the limited spectral range over which this region may exist. It is instructive to present an energy spectrogram: premultiplied spectra at 40 logarithmically spaced positions within the range $10.6 \lesssim z^+ \lesssim \delta^+$ are presented with iso-contours of $k_x^+\phi_{uu}^+$ in figure 1(*a*). These spectra were obtained from hot-wire measurements at $Re_\tau \approx 14\,100$ in Melbourne's TBL facility (Baars *et al.* 2017*a*). Near-wall streaks (Kline *et al.* 1967) dominate the inner-spectral peak in the TBL spectrogram (identified with the $\times$ marker at $\lambda_x^+ = 10^3$ and $z^+ = 15$), while large-scale organized motions induce a broad spectral peak in the log region, indicated with a $\times$ marker at $\lambda_x = 4\delta$ and $z^+ = 3.9Re_\tau^{1/2} \approx 464$ (Mathis, Hutchins & Marusic 2009). Nickels *et al.* (2005) determined a k_x^{-1} region as $z^+ > 100$, $\lambda_x > 15.7z$ (wall-scaling) and $\lambda_x < 0.3\delta$ (outer-scaling) at $Re_\tau \approx 14\,000$ (triangular region 'N' in figure 1*a*). This region satisfied (1.2) with $k_x^+\phi_{uu}^+ = A_1 \approx 0.92$. In Part 1 it was determined from a coherence analysis

(Baars, Hutchins & Marusic 2017*b*), relative to a wall-based reference, that wall-attached self-similar motions only become spectrally energetic at $\lambda_x \gtrsim 14z$. It is important to note here that this result was derived from a stochastic analysis of the streamwise velocity component only. It was furthermore suggested that $\phi_{uu} \propto k_x^{-1}$ is unlikely for $Re_\tau \lesssim 80\,000$. This is consistent with the study of Chandran *et al.* (2017), where experimentally acquired streamwise–spanwise two-dimensional spectra of u at $Re_\tau \sim O(10^4)$ were examined for a k_x^{-1}. They concluded that an appreciable k^{-1} scaling region can only appear for $Re_\tau \gtrsim 60\,000$. Moreover, even for the highest Re_τ laboratory data, the presence of a $\phi_{uu} \propto k_x^{-1}$ has been inconclusive (Morrison *et al.* 2002; Rosenberg *et al.* 2013; Vallikivi, Ganapathisubramani & Smits 2015), while this region must grow with Re_τ.

We now switch our attention to evidence for (1.1). A caveat in determining A_1 from $\overline{u^2}(z)$ profiles is that, generally, all turbulent scales are lumped together as one (integral of the entire spectrum). This approach inherently assumes that the attached-eddy structures dominate $\overline{u^2}$. Now, if one accepts that the attached-eddy contribution to the overall turbulence intensity grows with Re_τ, this assumption should become more valid. For this reason, Marusic *et al.* (2013) considered high Re_τ data in the range $2 \times 10^4 < Re_\tau < 6 \times 10^5$ (Hultmark *et al.* 2012; Hutchins *et al.* 2012; Winkel *et al.* 2012; Marusic *et al.* 2015) and inferred that $A_1 = 1.26$ (see figure 1*b*). It is worth noting that the value for A_1 has changed significantly over time. For instance, values for A_1 have been quoted as 1.03 (Perry & Li 1990), 1.26 (Hultmark *et al.* 2012; Marusic *et al.* 2013; Örlü *et al.* 2017) and 1.65 (Yamamoto & Tsuji 2018). These variations in A_1 are largely due to the varying TI slope with Re_τ and the different fitting regions for (1.1).

The previous discussion illustrates that A_1 values found from $\overline{u^2}$ profiles vary, while the AEH envisions a constant A_1 in (1.1): one that is invariant with Re_τ. Moreover, A_1 values found from $\overline{u^2}$ profiles do not agree with values for A_1 inferred from spectra via (1.2), despite the fact that this is expected per the attached-eddy model (Perry *et al.* 1986). A central facet of this mismatch is the simple fact that (1.1) and (1.2) are restricted to attached-eddy turbulence only, while in measures of the total streamwise turbulence kinetic energy more contributions are present. For a quantitative insight into what portion of the turbulence kinetic energy is representative of attached-eddy turbulence, a spectral decomposition method was introduced in Part 1 (and is summarized next).

1.2. *Streamwise energy spectra and the triple decomposition*

Data-driven spectral filters were empirically found with the aid of two-point measurements and a spectral coherence analysis. A first filter, denoted as $f_{\mathcal{W}}$, was based on a reference position deep within the near-wall region (or at the wall). Such a reference position allows us to determine the degree of coherence between the u fluctuations within the TBL and the fluctuations that are present at the reference position. The other filter, $f_{\mathcal{L}}$, was based on a reference position in the logarithmic region. It was verified that both spectral filters were universal for $Re_\tau \sim O(10^3) - O(10^6)$. Filter $f_{\mathcal{W}}$ was formulated as

$$f_{\mathcal{W}}^p(z;\lambda_x) = \begin{cases} 0, & \lambda_x < Rz, \\ \min\left\{ C_1 \ln\left(\dfrac{\lambda_x}{z}\dfrac{1}{R}\right),\ 1 \right\}, & Rz \leqslant \lambda_x \leqslant T_n\delta, \\ \min\left\{ C_1 \ln\left(\dfrac{T_n\delta}{z}\dfrac{1}{R}\right),\ 1 \right\}, & \lambda_x > T_n\delta. \end{cases} \tag{1.3}$$

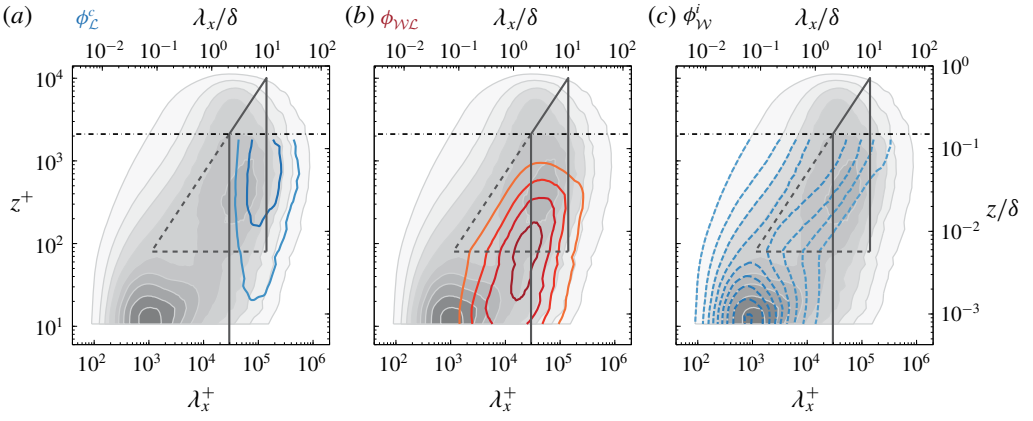

FIGURE 2. Dataset $\mathcal{W}$ with $Re_\tau \approx 14\,100$. (*a–c*) Premultiplied energy spectrograms of the three spectral sub-components (for $z < z_{\mathcal{L}}$), each of them overlaid on the total energy spectrogram (filled iso-contours 0.2 : 0.2 : 1.8). Following figure 14 of Part 1.

Subscript $\mathcal{W}$ signifies the wall-based reference, on which this filter is based, and the three constants are: $C_1 = 0.3017$, $R = 14.01$ and $T_n = 10$ (table 2, Part 1). A smooth filter $f_{\mathcal{W}}(z;\, \lambda_x)$ was generated by convoluting (1.3) with a log-normal distribution, $g(\lambda_x)$, spanning six standard deviations, corresponding to 1.2 decades in λ_x (details are provided in Part 1). Filter $f_{\mathcal{W}}(z;\, \lambda_x) \in [0,\, 1]$ and equals a wavelength-dependent fraction of energy that is stochastically coherent with the near-wall region. Consequently, $(1 - f_{\mathcal{W}})$ is the incoherent energy fraction. Filter $f_{\mathcal{L}}$ employs a reference position $z_{\mathcal{L}}$ in the logarithmic region,

$$f^p_{\mathcal{L}}(z_{\mathcal{L}};\, \lambda_x) = \begin{cases} 0, & \lambda_x < R' z_{\mathcal{L}}, \\ \min\left\{ C_1' \ln\left(\dfrac{\lambda_x}{z_{\mathcal{L}}} \dfrac{1}{R'} \right),\ 1 \right\}, & R' z_{\mathcal{L}} \leqslant \lambda_x \leqslant T_n \delta, \\ \min\left\{ C_1' \ln\left(\dfrac{T_n \delta}{z_{\mathcal{L}}} \dfrac{1}{R'} \right),\ 1 \right\}, & \lambda_x > T_n \delta. \end{cases} \tag{1.4}$$

Filter constants are $C_1' = 0.3831$, $R' = 13.18$ and $T_n = 10$. A smooth filter $f_{\mathcal{L}}(z_{\mathcal{L}};\, \lambda_x)$ was formed in a similar way as $f_{\mathcal{W}}(z;\, \lambda_x)$. Of the fraction of energy that is stochastically coherent with the near-wall region (via $f_{\mathcal{W}}$), a sub-fraction of that energy is also coherent with $z_{\mathcal{L}}$ in the logarithmic region (and this fraction is prescribed by $f_{\mathcal{L}}$).

A triple decomposition for ϕ_{uu} was formed from $f_{\mathcal{W}}$ and $f_{\mathcal{L}}$ (§ 5.1, Part 1), following

$$\phi^c_{\mathcal{L}}(z;\, \lambda_x) \equiv \phi_{uu}(z;\, \lambda_x) f_{\mathcal{L}}(z;\, \lambda_x), \tag{1.5}$$

$$\phi^i_{\mathcal{W}}(z;\, \lambda_x) \equiv \phi_{uu}(z;\, \lambda_x)[1 - f_{\mathcal{W}}(z;\, \lambda_x)], \tag{1.6}$$

$$\phi_{\mathcal{WL}}(z;\, \lambda_x) \equiv \phi_{uu}(z;\, \lambda_x)[f_{\mathcal{W}}(z;\, \lambda_x) - f_{\mathcal{L}}(z;\, \lambda_x)]. \tag{1.7}$$

Consequently, $\phi_{uu} = \phi^c_{\mathcal{L}} + \phi_{\mathcal{WL}} + \phi^i_{\mathcal{W}}$ and figure 2 illustrates this decomposition for $Re_\tau \approx 14\,100$ (duplicate of figure 14, Part 1). The three energy spectrograms of (1.5)–(1.7) are overlaid on the premultiplied energy spectrogram $k_x^+ \phi_{uu}^+$. Here,

$z_{\mathcal{L}} = 0.15\delta$ and the triple decomposition is performed for $z < z_{\mathcal{L}}$. In the near-wall region, here taken as $z^+ \lesssim z_T^+$ (nominally $z_T^+ = 80$ is used, approximately the wall-normal position at which the near-wall spectral peak becomes indistinguishable from the spectrogram), $f_{\mathcal{W}}$ is z-invariant and taken as $f_{\mathcal{W}}(z_T^+; \lambda_x)$. Throughout this work, the exact value of z_T^+ is of secondary importance, since small variations in this location do not affect the conclusions, given a lower bound of the logarithmic region in viscous-scaling, $z_T = O(100\nu/U_\tau)$. In § 2.2 of Part 1 we discussed that a classical scaling of the lower limit of the logarithmic region (as opposed to a mesolayer-type scaling via $z^+ \propto Re_\tau^{0.5}$) should not be discarded. In fact, in this paper we show that when we accept such a classical scaling, the growth of the near-wall peak in $\overline{u^2}$ can be explained via the increasingly intense energetic imprint of the Reynolds-number-dependent outer motions onto the near-wall region.

Component $\phi_{\mathcal{L}}^c$ (figure 2*a*) comprises the energy that is coherent via $f_{\mathcal{L}}$: large-scale wall-attached energy that is coherent with $z_{\mathcal{L}} = 0.15\delta$. This component includes spectral imprints of self-similar, wall-attached structures reaching beyond $z_{\mathcal{L}}$ and non-self-similar wall-attached structures that are coherent with $z_{\mathcal{L}}$ (e.g. some very large-scale motions (VLSMs)). Component $\phi_{\mathcal{W}}^i$ (figure 2*c*) is formed from the $f_{\mathcal{W}}$-based incoherent energy. This small-scale energy is wall detached and includes detached (non)-self-similar motions, such as phase-inconsistent attached eddies, incoherent VLSMs, etc. The remaining component, $\phi_{\mathcal{WL}}$, equals the wall-coherent energy below $z_{\mathcal{L}}$ and consists of self-similar and non-self-similar contributions. However, the non-self-similar contributions are likely to reside at large λ_x (reflecting global modes, Bullock, Cooper & Abernathy 1978; del Álamo & Jiménez 2003).

1.3. *Present contribution and outline*

Coming back to § 1.1, we can now argue that A_1 can be inferred from $\overline{u^2}(z)$ profiles via (1.1), as long as the streamwise TI contributions, other than that from the self-similar wall-attached motions, are removed. This step is crucial, because Part 1 already addressed that the other contributions (e.g. $\phi_{\mathcal{L}}^c$ in figure 2*a* and $\phi_{\mathcal{W}}^i$ in figure 2*c*) result in additions to the streamwise TI that constitute a clear z-dependence. And, the Reynolds-number-dependent outer-spectral peak seems to mask a possible $\phi_{uu} \propto k_x^{-1}$ (see spectra in Morrison *et al.* 2002; Nickels *et al.* 2005; Marusic *et al.* 2010*b*; Baidya *et al.* 2017; Samie *et al.* 2018). When re-assessing A_1 in this paper, both the spectral view and $\overline{u^2}(z)$ are considered simultaneously, while recognizing that A_1 must solely be associated with the turbulence that obeys the AEH.

Next, in §§ 2.1–2.2, decompositions of the streamwise TI are presented for a range of Re_τ. Data used are the same as in Part 1 (Baars & Marusic 2020, § 3.2). Findings on the Townsend–Perry constant A_1 are reconciled in § 2.3, after which its relation to the near-wall TI growth, with Re_τ, is presented in § 3. Empirical trends within the wall-normal profiles for all three additive sub-components of the streamwise TI are presented in § 4, together with a discussion of their scalings.

2. Decomposition of the streamwise turbulence intensity

2.1. *Methodology and logarithmic scalings*

Figure 3(*a*) shows the three sub-components $\phi_{\mathcal{L}}^c$, $\phi_{\mathcal{WL}}$ and $\phi_{\mathcal{W}}^i$ for the spectrum at $z^+ \approx 101$ (slice through figure 2). When integrated, these sub-components form three contributions to the streamwise TI, being $\overline{u^2}_{\mathcal{L}}$, $\overline{u^2}_{\mathcal{WL}}$ and $\overline{u^2}_{\mathcal{W}}$, respectively. In

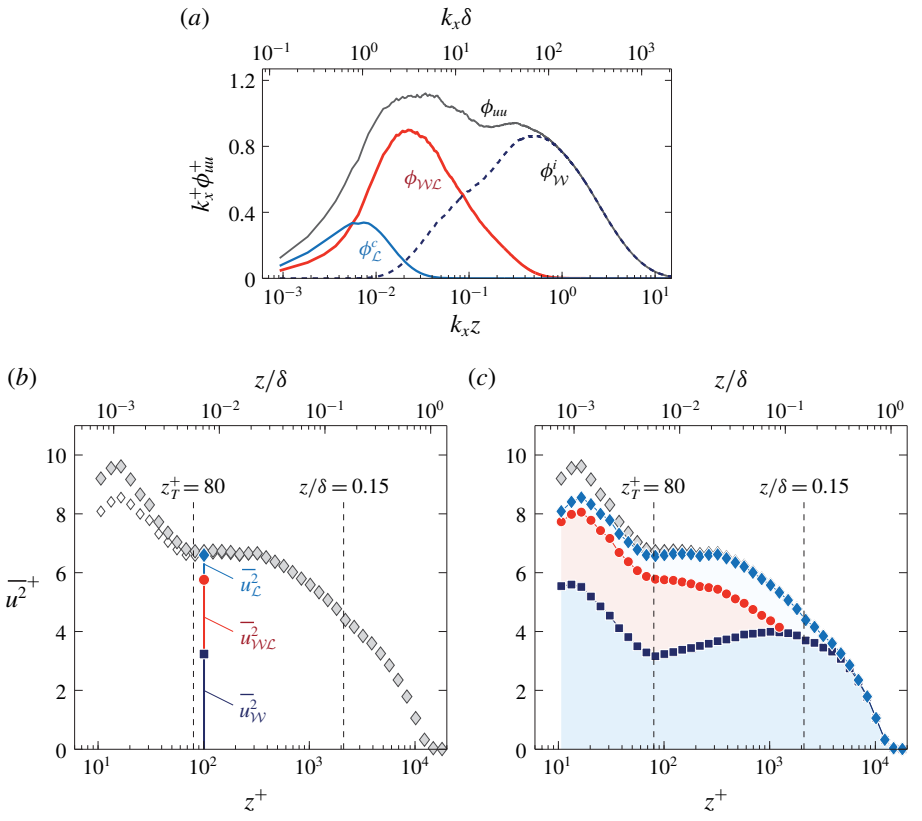

FIGURE 3. (*a*) Triple-decomposed energy spectrum at $z^+ \approx 101$ and $Re_\tau \approx 14\,100$, reproduced from figure 13(*e*) in Part 1. (*b*) Streamwise TI profile with the three TI sub-components following (2.2). (*c*) Similar to (*b*) but for all wall-normal locations.

summary,

$$\overline{u^2}(z) = \int \phi_{uu}(z; k_x)\,\mathrm{d}k_x \tag{2.1}$$

$$= \underbrace{\int \phi^i_{\mathcal{W}}(z; k_x)\,\mathrm{d}k_x}_{\overline{u^2}_{\mathcal{W}}} + \underbrace{\int \phi_{\mathcal{WL}}(z; k_x)\,\mathrm{d}k_x}_{\overline{u^2}_{\mathcal{WL}}} + \underbrace{\int \phi^c_{\mathcal{L}}(z; k_x)\,\mathrm{d}k_x}_{\overline{u^2}_{\mathcal{L}}}. \tag{2.2}$$

Figure 3(*b*) presents these three sub-components of the TI at $z^+ \approx 101$, together with $\overline{u^2}(z)$ (open diamonds). Wall-normal profiles of the three sub-components are obtained when this integration is performed for each z (figure 3*c*). Note that the contributions are shown in a cumulative format; the bottom profile (squares) represents $\overline{u^2}_{\mathcal{W}}$, the intermediate profile (circles) encompasses $\overline{u^2}_{\mathcal{W}} + \overline{u^2}_{\mathcal{WL}}$, whereas the final profile (diamonds), $\overline{u^2}_{\mathcal{W}} + \overline{u^2}_{\mathcal{WL}} + \overline{u^2}_{\mathcal{L}}$, equals $\overline{u^2}$ by construction. Regarding the full $\overline{u^2}(z)$ profile, it is well known that the near-wall streamwise TI is attenuated due to spatial resolution effects of hot-wires (Hutchins *et al.* 2009). Here the spanwise width of

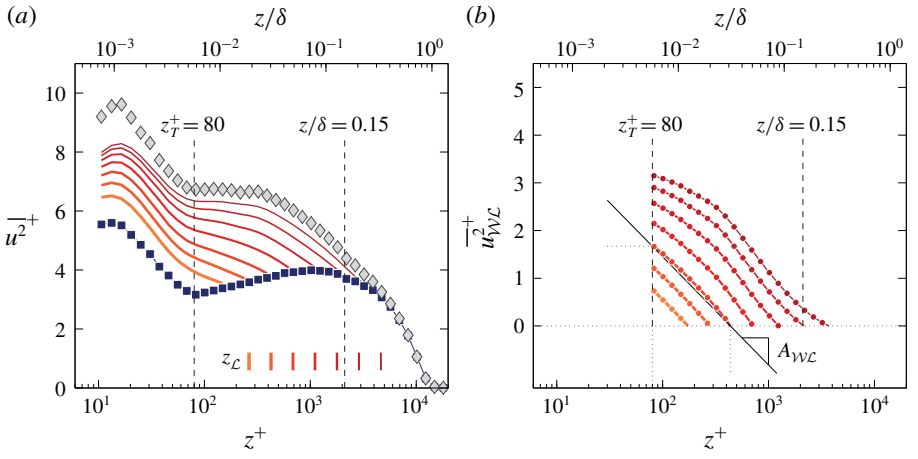

FIGURE 4. (*a*) Streamwise TI at $Re_\tau \approx 14\,100$. Component $\overline{u^2}_{\mathcal{W}}$ is shown with the square symbols, while the sequence of lines with increasing colour intensity represents $\overline{u^2}_{\mathcal{W}} + \overline{u^2}_{\mathcal{WL}}$ for increasing $z_{\mathcal{L}}$; locations of $z_{\mathcal{L}}$ are indicated with the vertical lines. (*b*) Profiles of $\overline{u^2}^+_{\mathcal{WL}}$.

the hot-wire sensing length was $l^+ \approx 22$. A corrected profile for the streamwise TI is superposed in figure 3(*b*) with filled diamonds, following the method of Smits, McKeon & Marusic (2011). Samie *et al.* (2018) confirmed that this correction scheme is valid for Reynolds numbers up to $Re_\tau \approx 20\,000$. Because the TI above the near-wall region (say $z > z_T$) is unaffected by spatial resolution issues, we proceed our analysis without hot-wire corrections.

The wall-incoherent component, $\overline{u^2}_{\mathcal{W}}$, exhibits an increase in its energy magnitude with increasing z throughout the logarithmic region. Section 4 addresses the wall-normal trend of this TI component in more detail. Components $\overline{u^2}_{\mathcal{WL}}$ and $\overline{u^2}_{\mathcal{L}}$ have to be considered in relation to one another. Figure 4(*a*) illustrates the dependence of the two TI sub-components on $z_{\mathcal{L}}$, by presenting $\overline{u^2}_{\mathcal{W}}$ (squares) and $\overline{u^2}_{\mathcal{W}} + \overline{u^2}_{\mathcal{WL}}$ (lines) for a range of $z_{\mathcal{L}}$ (indicated with the vertical lines). Part 1 addressed how their spectral equivalents, $\phi_{\mathcal{WL}}$ and $\phi^c_{\mathcal{L}}$, varied with $z_{\mathcal{L}}$ and here we describe what implications that has on the streamwise TI. At low $z_{\mathcal{L}}$, the wall-attached motions smaller than $z = z_{\mathcal{L}}$ contribute to $\phi_{\mathcal{WL}}$, but the wall-normal range of $\phi_{\mathcal{WL}}$ is limited (per definition, $\phi_{\mathcal{WL}}$ is non-existent above $z_{\mathcal{L}}$). With increasing $z_{\mathcal{L}}$, the range of wall-attached motions increases, but global modes (or imprints of non-self-similar VLSMs/superstructures) that are restricted to $z < z_{\mathcal{L}}$ also start to contribute significantly to $\phi_{\mathcal{WL}}$ (due to the inherent difficulty in spectrally decomposing the two, see § 5.2 in Part 1). Hence, $\phi_{\mathcal{WL}}$ does not just contain energy from wall-attached self-similar motions. When $z_{\mathcal{L}}$ resides in the intermittent region, all global modes are being assigned to $\phi_{\mathcal{WL}}$ (and thus to $\overline{u^2}_{\mathcal{WL}}$). This is reflected by the highest $z_{\mathcal{L}}$ profile in figure 4(*a*); in the process of increasing $z_{\mathcal{L}}$, a hump has appeared in the streamwise TI (approaching $\overline{u^2}$ for $z_{\mathcal{L}} \to \delta$).

We now focus exclusively on $\overline{u^2}_{\mathcal{WL}}$ as this sub-component is closely aligned with the scaling following (1.1). Figure 4(*b*) shows $\overline{u^2}_{\mathcal{WL}}$ for $z^+ > z_T^+$ (the near-wall TI is irrelevant in this discussion). Although it was pointed out above that wall-normal profiles of $\overline{u^2}_{\mathcal{WL}}$ do comprise a signature of wall-attached non-self-similar motions, two trends of its statistics are reflective of wall-attached self-similar motions:

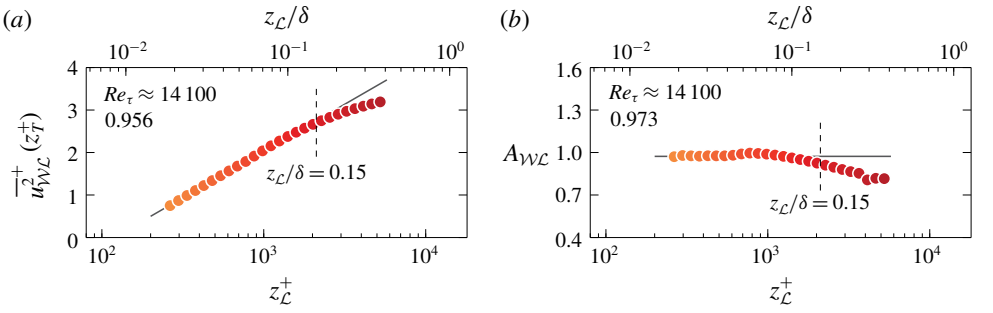

FIGURE 5. (*a*) Value of $\overline{u^2}^+_{\mathcal{WL}}$ at $z_T^+ = 80$ from figure 4(*b*); the line, following (2.3), is the fit to the data at $z_\mathcal{L} < 0.15\delta$ (its slope $A'_{\mathcal{WL}}$ is listed). (*b*) Value of $A_{\mathcal{WL}}$, as indicated in figure 4(*b*), superposed on the line corresponding to its mean for data at $z_\mathcal{L} < 0.15\delta$ (value listed).

(i) First, the magnitude of $\overline{u^2}_{\mathcal{WL}}$ at z_T is displayed in figure 5(*a*), with $z_\mathcal{L}$ forming the abscissa (with a finer $z_\mathcal{L}$-discretization than used in figure 4). When assuming that the non-self-similar, large-scale motions have a negligible influence on the TI-trend at z_T, and that $\overline{u^2}_{\mathcal{WL}}$ obeys Townsend's AEH, we arrive at

$$\overline{u^2}_{\mathcal{WL}} \propto A'_{\mathcal{WL}} \ln\left(\frac{z_\mathcal{L}}{\delta}\right). \tag{2.3}$$

That is, an increase of $z_\mathcal{L}$ mimics an increase in Re_τ through the inclusion of more wall-attached scales in $\overline{u^2}_{\mathcal{WL}}$. Data in figure 5(*a*) adhere to (2.3) for approximately one decade in $z_\mathcal{L}$ and fitting of the data at $z_\mathcal{L} < 0.15\delta$ results in $A'_{\mathcal{WL}} \approx 0.956$ (note that $z_\mathcal{L} = 0.15\delta$ is often taken as the upper edge of the logarithmic region).

(ii) A second measure that is reflective of self-similar wall-attached motions is the decay of $\overline{u^2}_{\mathcal{WL}}(z)$ following (1.1), which is now used to quantify the trend in $\overline{u^2}_{\mathcal{WL}}$. It is impossible to perform a direct fit of a logarithmic decay to the data of $\overline{u^2}_{\mathcal{WL}}$ in figure 4(*b*), because of the aforementioned issues (for large $z_\mathcal{L}$, the profiles are influenced by non-self-similar, global-mode turbulence). Instead, a logarithmic slope $A_{\mathcal{WL}}$ is defined from the two endpoints of the profile, $\overline{u^2}_{\mathcal{WL}}(z_T)$ and $\overline{u^2}_{\mathcal{WL}} = 0$, via

$$A_{\mathcal{WL}} \equiv \frac{\overline{u^2}_{\mathcal{WL}}(z_T^+)}{\ln\left(z^+|_{\overline{u^2}_{\mathcal{WL}}=0}\right) - \ln(z_T^+)}. \tag{2.4}$$

Figure 4(*b*) displays the logarithmic slope for one profile (discrete point measurements were interpolated to exactly $z_T^+ = 80$ and the z^+ position at which $\overline{u^2}_{\mathcal{WL}}$ becomes zero). Data in figure 5(*b*), and their mean value $A_{\mathcal{WL}} \approx 0.973$, are in close agreement to $A'_{\mathcal{WL}} \approx 0.956$ from figure 5(*a*). This is expected when $\overline{u^2}_{\mathcal{WL}}$ obeys an attached-eddy scaling.

2.2. *Reynolds-number variation*

We now assess how the identified logarithmic scalings via (2.3) and (2.4) depend on the Reynolds number. Single-point hot-wire measurements at a range of Reynolds

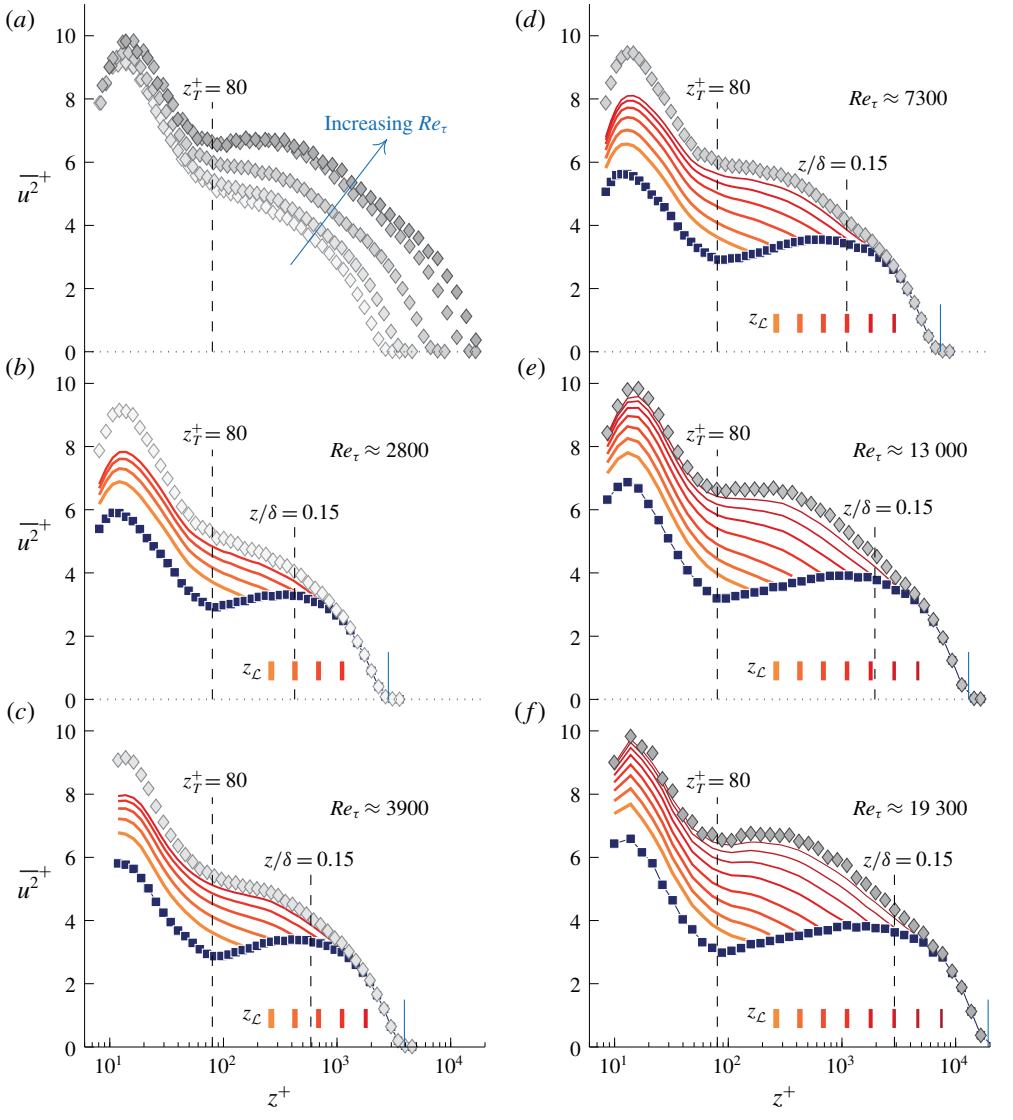

FIGURE 6. (*a*) Streamwise TI profiles for $Re_\tau \approx 2800$, 3900 and 7300 (Hutchins *et al.* 2009) and $Re_\tau \approx 13\,000$ and 19 000 (Samie *et al.* 2018). (*b–f*) Profiles of (*a*) decomposed into various TI sub-components: $\overline{u^2}_\mathcal{W}$ is shown with the square symbols, while the sequence of lines with increasing colour intensity represents $\overline{u^2}_\mathcal{W} + \overline{u^2}_{\mathcal{W}\mathcal{L}}$ for increasing $z_\mathcal{L}$ (similar to figure 4*a*).

numbers were employed in § 6 of Part 1 to address the Reynolds-number variation of the triple-decomposed energy spectrograms. These same single-point hot-wire data are here processed via the procedure described previously (§ 2.1). First, the $\overline{u^2}(z)$ profiles for these data are shown in figure 6(*a*). For the three lowest Reynolds numbers ($Re_\tau \approx 2800$, 3900 and 7300: Hutchins *et al.* (2009)), data were corrected for spatial attenuation effects (Smits *et al.* 2011), whereas the two other profiles ($Re_\tau \approx 13\,000$ and 19 300: Samie *et al.* (2018)) comprise fully resolved measurements. An energy

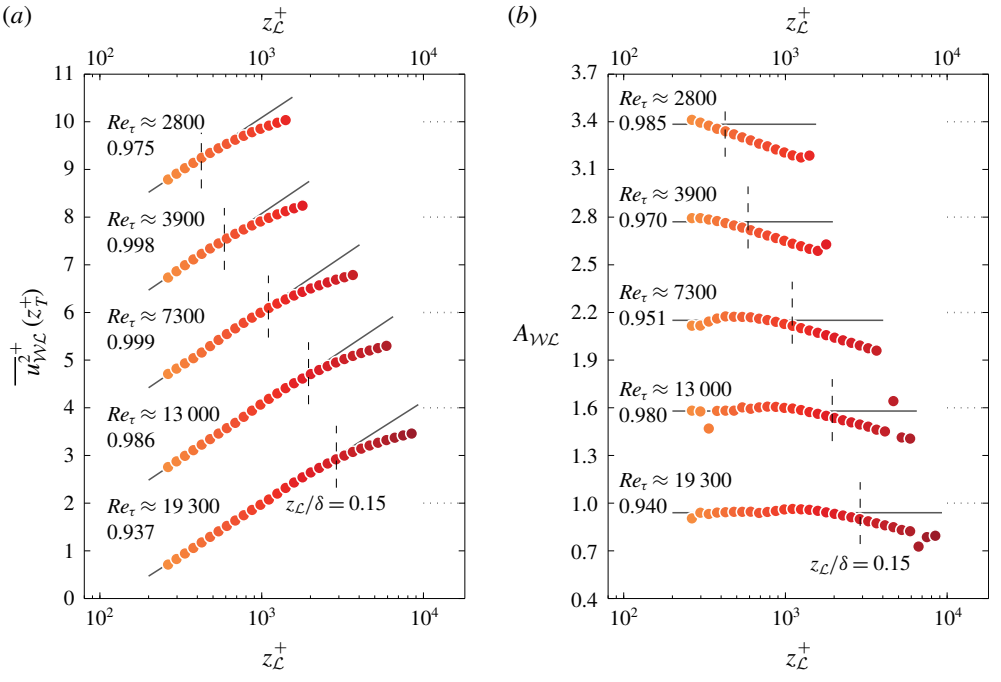

FIGURE 7. (*a*) Value of $\overline{u^2}^+_{\mathcal{WL}}$ at $z_T^+ = 80$ from figure 6(*b–f*); lines, following (2.3), are fit to the data at $z_{\mathcal{L}} < 0.15\delta$ (their slopes $A'_{\mathcal{WL}}$ are listed). (*b*) Value of $A_{\mathcal{WL}}$, superposed on the line corresponding to its mean value for data at $z_{\mathcal{L}} < 0.15\delta$ (values listed). Each subsequent Re_τ case is vertically offset by 2 and 0.6, starting with the second from the bottom, in (*a*) and (*b*), respectively.

growth in the outer region presents itself through the emergence of a local maximum in $\overline{u^2}$ (Samie *et al.* 2018), whereas at the same time, the near-wall TI grows with Re_τ (Marusic, Baars & Hutchins 2017).

Data of each Reynolds-number case are spectrally decomposed to generate a similar output as presented in figure 4(*a*). For each of the five Re_τ profiles in figure 6(*a*), the result is shown in figure 6(*b–f*). Additionally, with the aid of (2.3) and (2.4), figure 5(*a*,*b*) is constructed for each of the five Reynolds numbers, as shown in figure 7(*a*,*b*).

Especially at the two largest Reynolds numbers ($Re_\tau \approx 13\,000$ and 19 300), there is a consistent agreement between $A_{\mathcal{WL}}$ and $A'_{\mathcal{WL}}$, which is indicative of the slopes being a reflection of attached-eddy type turbulence. At the two lowest Reynolds numbers ($Re_\tau \approx 2800$ and 3900), the $A_{\mathcal{WL}}$ slope extracted from the two profile endpoints of $\overline{u^2}_{\mathcal{WL}}$ exhibits a decreasing trend (top two profiles in figure 7*b*). This is ascribed to the fact that the upward trend of $\overline{u^2}_{\mathcal{W}}$ (square symbols in figures 6*b*,*c*) changes rapidly near the upper edge of the logarithmic region: its magnitude starts to decrease around $z/\delta \approx 0.15$ in order to merge with the TI profiles in the wake region. Because of this decrease, there is a less rapid decay of the $\overline{u^2}_{\mathcal{WL}}$ profiles near $z/\delta \approx 0.15$. When slope $A_{\mathcal{WL}}$ is determined from the two profile endpoints, it causes a decreased slope. Generally, the limited scale separation in the triple-decomposed spectrograms at low Reynolds numbers exacerbates this issue (see also the spectrograms in figure 18 of Part 1).

2.3. *Reconciling A_1 from trends in the turbulence intensity and spectra*

Having re-assessed the wall-normal decay of the TI sub-component associated with Townsend's attached eddies (§§ 2.1–2.2), we can now proceed with reconciling the status quo. Recall that (1.1) is restricted to the streamwise TI that is generated by inviscid, geometrically self-similar and wall-attached eddies only. Because both $A'_{\mathcal{WL}}$ and $A_{\mathcal{WL}}$ were inferred by considering the sub-component of the TI that complies with Townsend's assumptions only, those slopes are interpreted as A_1. Figure 8 displays $A'_{\mathcal{WL}}$, for all Reynolds numbers, with the open square symbols. Uncertainty estimates are shown with the error bars and are based on 95 % confidence bounds from the fitting procedure of (2.3). Alongside, with the solid square symbols, values of $A_{\mathcal{WL}}$ are shown with the uncertainty estimates based on the 95 % confidence interval of the data points residing at $z_{\mathcal{L}} < 0.15\delta$ in figures 5(*b*) and 7(*b*). Numerical values are summarized in table 1. To complete quantification of (1.1) by considering $\overline{u^2}_{\mathcal{WL}}$ energy only, offset B_1 can be determined. For this we have to introduce a new quantity $\overline{u^2}_{AE}$, which is the TI decay with a pure logarithmic decay,

$$\overline{u^2}^+_{AE}(z/\delta) = B_1(z_{\mathcal{L}} = 0.15\delta) - A_1 \ln\left(\frac{z}{\delta}\right), \quad \text{for } z^+ \geqslant z_T^+. \tag{2.5}$$

Although offset B_1 depends on $z_{\mathcal{L}}$ (see figure 4*b*), we only have to consider the scenario for one specific $z_{\mathcal{L}}$ to infer its Reynolds-number trend (here we take $z_{\mathcal{L}} = 0.15\delta$). Values for $B_1(z_{\mathcal{L}} = 0.15\delta)$ are shown on the bottom of figure 8. Mean values for both A_1 and B_1 are found from the mean values of $A_1 = A'_{\mathcal{WL}}$ and B_1 in table 1, resulting in

$$A_1 = 0.975, \quad B_1(z_{\mathcal{L}} = 0.15\delta) = -2.267. \tag{2.6a,b}$$

To indicate the effect of the variation in A_1 and B_1 with Re_τ, six lines according to formulation (2.5), with the six values of $A_1 = A'_{\mathcal{WL}}$ and B_1 (down to $z_T^+ = 80$) are shown in the inset in figure 8, together with the TI profiles of figure 6(*a*). The scatter in A_1 and B_1 (as well as the uncertainty estimates from the fitting procedure, listed in table 1), result in indistinguishable logarithmic trends in relation to typical experimental uncertainty in the TI profiles (e.g. Winkel *et al.* 2012; Vincenti *et al.* 2013; Marusic *et al.* 2017; Örlü *et al.* 2017; Samie *et al.* 2018). Both A_1 and B_1 are thus considered to be Reynolds-number invariant for $2800 \lesssim Re_\tau \lesssim 19\,300$.

A last set of data points in figure 8 comprises the peak values of $k_x^+\phi^+_{\mathcal{WL}}$ at $z^+ = 100$, duplicated from figure 20 in Part 1. These data consider A_1 in the context of the energy spectra. Because the scale separation in spectral space is still relatively limited at these Reynolds numbers, the peak value in the associated spectra ($k_x^+\phi^+_{\mathcal{WL}}$) keeps maturing with Re_τ (detailed in § 6.2, Part 1). At $Re_\tau \approx 19\,300$ there is a consistency between the value for A_1 found from the TI trend and the peak/plateau in the associated spectrum. However, it is acknowledged that no complete similarity has been observed in the associated $\phi_{\mathcal{WL}}$ spectra (e.g. figure 19, Part 1). Furthermore, the three Princeton HRTF data points of the peak in the $\phi_{\mathcal{WL}}$ spectrum are not conclusive on whether the spectral peak plateaus. The difficult conditions in the Princeton HRTF and the challenging aspects associated with the acquisition of repeatable statistics with miniature hot-wire probes (e.g. Samie *et al.* 2018) require more research to settle this issue. Only fully resolved, higher-Reynolds-number data at $z^+ = O(100)$ can provide definitive answers on whether a distinguished k_x^{-1} region develops (in which case the peak has to plateau to a Reynolds-number-invariant A_1, consistent

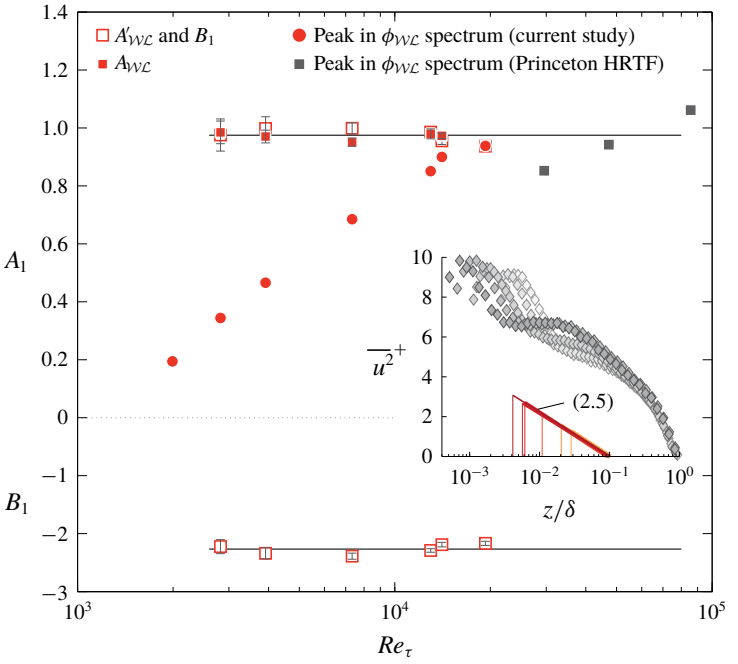

FIGURE 8. Values of $A'_{\mathcal{WL}}$ and $A_{\mathcal{WL}}$, alongside the peak values of $k_x^+\phi_{\mathcal{WL}}^+$ (duplicated from figure 20, Part 1). Values of B_1 are plotted at the bottom. TI profiles of figure 6(*a*) are shown in the inset, together with (2.5) for all six cases of $A_1 = A'_{\mathcal{WL}}$ and B_1.

	Turbulence intensity-based					Spectrum-based	
Re_τ	$A'_{\mathcal{WL}}$	$A_{\mathcal{WL}}$	Part,§	B_1	Section	$k_x^+\phi_{uu}^+\|_{peak}$	Part,§
2 000	—	—	—	—	—	0.195	1, § 1.1
2 800	0.975 ± 0.056	0.985 ± 0.040	2, § 2.2	-2.224 ± 0.122	2, § 2.3	0.344	1, § 6.2
3 900	0.998 ± 0.041	0.970 ± 0.022	2, § 2.2	-2.340 ± 0.095	2, § 2.3	0.466	1, § 6.2
7 300	0.999 ± 0.020	0.951 ± 0.014	2, § 2.2	-2.388 ± 0.053	2, § 2.3	0.685	1, § 6.2
13 000	0.986 ± 0.010	0.980 ± 0.017	2, § 2.2	-2.290 ± 0.030	2, § 2.3	0.851	1, § 6.2
14 100	0.956 ± 0.013	0.973 ± 0.010	2, § 2.1	-2.189 ± 0.038	2, § 2.3	0.900	1, § 6.2
19 300	0.937 ± 0.011	0.940 ± 0.009	2, § 2.2	-2.168 ± 0.036	2, § 2.3	0.938	1, § 6.2

TABLE 1. Values of $A'_{\mathcal{WL}}$, $A_{\mathcal{WL}}$ and B_1, which were inferred from the $\overline{u^2}_{\mathcal{WL}}$ profiles. Uncertainty estimates for $A_1 = A'_{\mathcal{WL}}$ and B_1 are based on 95 % confidence bounds from the fitting of (2.5), while the uncertainty estimates for $A_{\mathcal{WL}}$ are based on the 95 % confidence interval of the data points residing at $z_{\mathcal{L}} < 0.15\delta$ in figures 5(*b*) and 7(*b*).

with the TI trends). In the interim, figure 8 does not exclude that possibility: a rough extrapolation of the $\phi_{\mathcal{WL}}$ peak values approaches $A_1 \approx 1$, consistent with (2.6). Finally, to the authors' knowledge, our current work indicates for the first time that a Reynolds-number-invariant A_1 could be consistent with a potential k_x^{-1} at ultra-high Re_τ. Previously, $A_1 = 1.03$ (Perry & Li 1990; Marusic & Kunkel 2003) found from $\overline{u^2}(z)$ profiles was in close agreement with the spectral-based value of $A_1 \approx 0.95$ by Nickels *et al.* (2005), but this was strictly coincidental. The former was

obtained at significantly lower Reynolds numbers (highest $Re_\tau \approx 4400$) than the latter ($Re_\tau \approx 14\,000$).

3. Value of A_1 in relation to the turbulence intensity in the near-wall region

Consistent scaling laws have recently emerged for the inner peak of the streamwise TI. Samie *et al.* (2018) considered the maximum in the TI profiles, denoted as $\overline{u^2}_{max}$, from direct numerical simulation (DNS) data and fully resolved measurement data, to conclude that

$$\overline{u^2}^+_{max} = C + A_{max} \ln(Re_\tau), \tag{3.1}$$

with $C = 3.54$ and $A_{max} = 0.646$. Nominally, the maxima reside at $z^+_{max} = 15$. Lee & Moser (2015) observed (3.1) through DNS channel flow up to $Re_\tau \approx 5200$ and an increase of $\overline{u^2}^+_{max}$ with Re_τ is consistent with earlier studies (DeGraaff & Eaton 2000; Hutchins *et al.* 2009; Klewicki 2010). Peak values of the streamwise TI at z_{max}, as a function of Re_τ, are shown in figure 9. DNS data include the channel flow of Lee & Moser (2015) and TBL flow of Sillero, Jiménez & Moser (2013). Experimental data of TBLs are from studies performed in Melbourne's boundary layer facility (Marusic *et al.* 2015; Samie *et al.* 2018), UNH's Flow Physics Facility (Vincenti *et al.* 2013) and at Utah SLTEST (Metzger *et al.* 2001). All these data (aside from Samie *et al.* 2018) were corrected for spatial resolution effects via Smits *et al.* (2011). Atmospheric surface layer (ASL) data of Metzger *et al.* (2001), with a relatively small hot-wire length of $l^+ \lesssim 10$, are uncorrected (Hutchins *et al.* 2009). High-Reynolds-number experimental pipe flow data are also included from the CICLoPE facility (Örlü *et al.* 2017; Willert *et al.* 2017), reaching up to $Re_\tau \approx 40\,000$. Hot-wire data of Örlü *et al.* (2017) were again corrected for spatial resolution effects, whereas the particle image velocimetry (PIV) data of Willert *et al.* (2017) were nearly fully resolved. Given the measurement uncertainty, (3.1) appears to represent the trend well for all the data (solid line).

Figure 9 also presents $\overline{u^2}$ at $z_T^+ = 80$, except for the unavailable Utah SLTEST data at this location. When the data at $z_T^+ = 80$ adhere to an attached-eddy scaling, the Reynolds-number growth of the streamwise TI can be described by A_1, since (1.1) or (2.5) can be reformulated as

$$\overline{u^2}^+(z_T^+) = D + A_1 \ln(Re_\tau). \tag{3.2}$$

When fitting (3.2) to the data in figure 9 with $A_1 = 0.975$ (2.6), the offset constant D is determined as $D = -2.60$. Figure 9 shows that (3.2) represents the data well, meaning that the Reynolds-number behaviour of the streamwise TI, at a lower bound of the logarithmic region fixed in viscous-scaling, e.g. $80\nu/U_\tau$, is predicted well through an attached-eddy scaling alone. This thus implies that energy footprints from large-scale, global-mode VLSMs and small-scale wall-incoherent turbulence (reflected in $\overline{u^2}_{\mathcal{L}}$ and $\overline{u^2}_{\mathcal{W}}$, respectively) do not, or negligibly, contribute to the Reynolds-number trend over the range of Re_τ investigated here. That is, an energetic footprint is still present (clearly observed in component $\phi^c_{\mathcal{L}}$ in figure 2*c*, for instance), but its Reynolds-number trend seems weak as an attached-eddy scaling of self-similar turbulence alone can explain the growth of the streamwise TI at z_T and $z^+ = 15$. Interactions between the outer- and inner-region turbulence, however, are not insignificant. They are most pronounced in the near-wall region due to the co-existence of near-wall turbulence

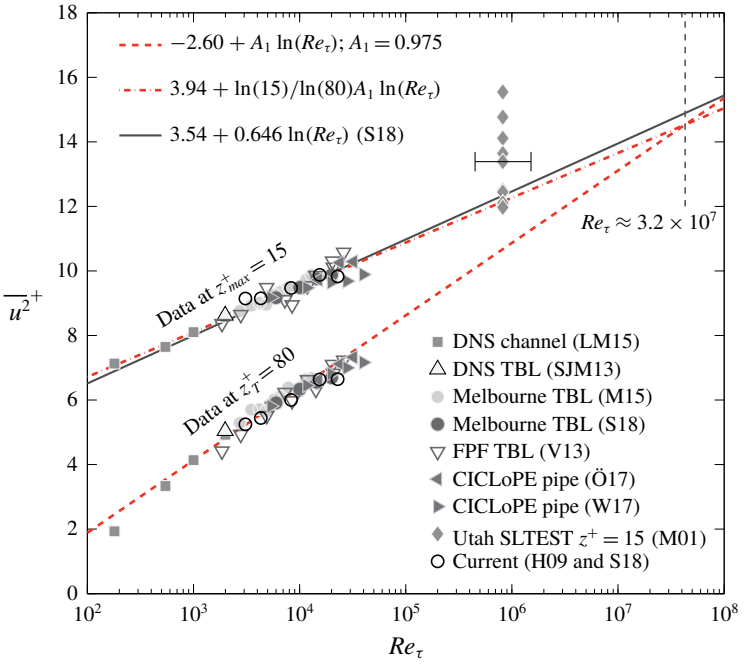

FIGURE 9. Turbulence intensity, $\overline{u^2}$, at the nominal wall-normal location of the inner peak, $z^+_{max} = 15$, and at $z^+_T = 80$. For the z^+_T data, a dashed line shows a Reynolds-number growth according to the attached-eddy scaling with $A_1 = 0.975$ (2.6*a*,*b*). For the z^+_{max} data, the dash-dotted line has a slope of $\ln(15)/\ln(80)A_1 = 0.603$, while the solid line represents (3.1). Data are from LM15: Lee & Moser (2015), SJM13: Sillero *et al.* (2013), M15: Marusic *et al.* (2015), S18: Samie *et al.* (2018), V13: Vincenti *et al.* (2013), Ö17: Örlü *et al.* (2017), W17: Willert *et al.* (2017), M01: Metzger *et al.* (2001) and H09: Hutchins *et al.* (2009).

and energetic footprints of larger-scale, wall-attached outer motions (e.g. Marusic *et al.* 2010*a*; Cho, Hwang & Choi 2018).

The question now remains how (3.1) and (3.2) are compatible (or how $A_{max} = 0.646$ is consistent with $A_1 = 0.975$). Marusic & Kunkel (2003) proposed that the near-wall viscous region is influenced by the Reynolds-number-dependent, outer-layer streamwise TI. The validity of this proposition was strengthened by the superposition framework detailed in the literature (Hutchins & Marusic 2007; Marusic *et al.* 2010*a*; Mathis, Hutchins & Marusic 2011; Baars, Hutchins & Marusic 2016) and studies focusing on a near-wall component that is free of motions not scaling in inner units (e.g. Hu & Zheng 2018). Note, however, that a complex scale interaction and spectral energy transfer are present (de Giovanetti, Sung & Hwang 2017; Cho *et al.* 2018), in combination with an outer motion wall-shear-stress footprint (Abe, Kawamura & Choi 2004; de Giovanetti, Hwang & Choi 2016). In summary, we move forward with the near-wall TI being composed of two contributions:

(i) A universal function that is Reynolds-number invariant when scaled in inner units, denoted as $\overline{u^2}^+_{NW}(z^+)$. It mainly encompasses the inner peak in the spectrogram induced by the near-wall cycle (NW cycle), but also comprises a contribution

– that seems to be Reynolds-number invariant – from the largest, outer-region motions (see our discussion above).

(ii) An additive component that accounts for the Reynolds-number-dependent superposition of the outer-region TI onto the near-wall viscous region. It is hypothesized that this Reynolds-number dependence is solely the result of the attached-eddy turbulence at $z_T^+ = 80$. In simplest form, it can be hypothesized that the near-wall footprint drops off linearly in $\ln(z^+)$, to zero at $z^+ = 1$, so that

$$\overline{u^2}^+_{AE}(z^+, Re_\tau) = \frac{\ln(z^+)}{\ln(z_T^+)}\overline{u^2}^+_{AE}(z_T^+), \quad \text{for } 1 \leqslant z^+ \leqslant z_T^+, \tag{3.3}$$

where $\overline{u^2}^+_{AE}(z_T^+)$ is found from (2.5), which is reformulated as

$$\overline{u^2}^+_{AE}(z_T^+) = [B_1(z_{\mathcal{L}} = 0.15\delta) - A_1 \ln(z_T^+)] + A_1 \ln(Re_\tau). \tag{3.4}$$

As $\overline{u^2}^+_{NW}(z^+)$ is Reynolds-number invariant, $\overline{u^2}^+(z^+_{max})$ grows with Re_τ via (3.1) with $A_{max} = \ln(z^+_{max})/\ln(z_T^+)A_1 = 0.603$. Refitting of (3.1) yields $C = 3.94$; figure 9 indicates that these constants represent the scattered data equally well as with $A_{max} = 0.646$ and $C = 3.54$ (adopted earlier from Samie *et al.* 2018). In order to extend the scaling validation to the entire near-wall region (not just z_{max}), reference DNS data of a zero pressure gradient (ZPG) TBL are utilized (Sillero *et al.* 2013). Figure 10(*a*) displays $\overline{u^2}$ from the DNS at $Re_\tau = 1990$. Following (3.3), part of this near-wall TI is envisioned as the attached-eddy component, labelled as $\overline{u^2}_{AE}$. The remaining TI forms $\overline{u^2}_{NW}$. For any Re_τ, data must now collapse when the near-wall attached-eddy contribution is subtracted from the near-wall TI profile. Figure 10(*b*) visualizes this assessment: the dashed line corresponds to $\overline{u^2}_{NW}$ from the DNS in figure 10(*a*), the symbols correspond to the five Reynolds-number profiles of figure 6(*a*) and the 10 blue-coloured profiles span $2800 < Re_\tau < 13\,400$ (taken from Marusic *et al.* 2017, where data were also corrected for the hot-wire's spatial attenuation effects). The excellent collapse of all data agrees with the two-part model, $\overline{u^2}(z^+, Re_\tau) = \overline{u^2}_{NW}(z^+) + \overline{u^2}_{AE}(z^+, Re_\tau)$. In conclusion, $A_1 = 0.975$ is consistent with the Reynolds-number increase of the near-wall TI.

4. Empirical trends in the decomposed turbulence intensity

Evidence for a portion of the streamwise TI in the logarithmic region adhering to (1.1) was provided in § 2. Subsequently, § 3 highlighted its consistency with the near-wall region scaling trends. In this section we proceed with an examination of the empirical trends in the decomposed TI, based on the explicit assumption that the attached-eddy turbulence obeys a perfect logarithmic decay with z. Following the data-driven spectral decomposition, the streamwise TI was earlier analysed in terms of its three additive components, following (2.2):

$$\overline{u^2}^+ = \overline{u^2}^+_{\mathcal{W}} + \overline{u^2}^+_{\mathcal{WL}} + \overline{u^2}^+_{\mathcal{L}}. \tag{4.1}$$

Wall-coherent components $\overline{u^2}_{\mathcal{WL}}$ and $\overline{u^2}_{\mathcal{L}}$, computed by the data-driven approach, are not separable in the sense that one of these consists of attached-eddy turbulence only (the inherent difficulty of decomposing energy wall-coherent self-similar attached

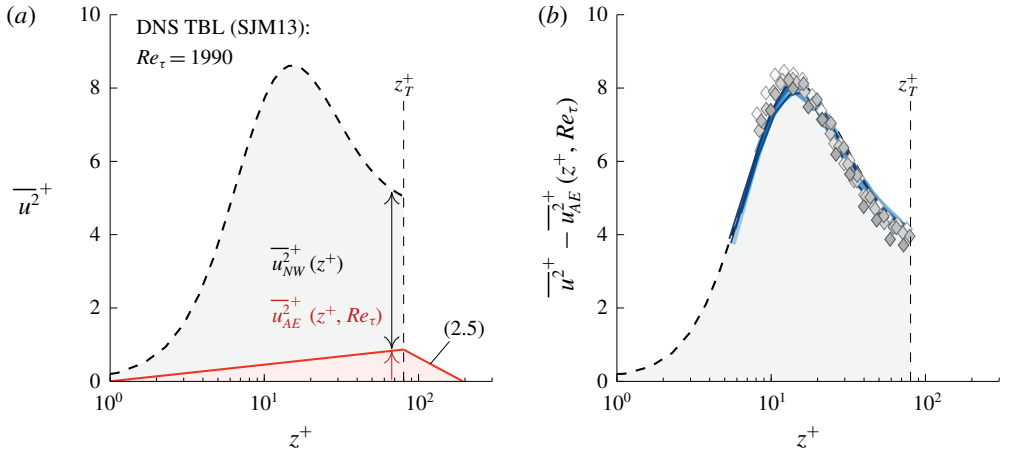

FIGURE 10. (*a*) Streamwise TI profile at $Re_\tau = 1990$ (DNS, Sillero *et al.* 2013), together with (3.3) and (2.5). (*b*) Streamwise TI profiles in the near-wall region, with the superposition component of the attached-eddies removed. Dashed line: DNS profile of (*a*), markers: data from figure 7(*a*), blue-coloured lines: 10 profiles from figure 7 in Marusic *et al.* (2017), spanning $2800 < Re_\tau < 13\,400$.

eddies from that of wall-coherent, large-scale non-self-similar motions was discussed in § 5.2 of Part 1). However, it was shown that $\overline{u^2}_{\mathcal{WL}}$ closely represents the energy content associated with attached eddies, by framing both (2.5) and (2.6). We now proceed with the explicit assumption that (2.5) exists and investigate the implications of this on the scaling of the sub-components, still totalling the non-decomposed TI, $\overline{u^2}$. First we replace $\overline{u^2}_{\mathcal{WL}}$ with $\overline{u^2}_{AE}$ (e.g. $\overline{u^2}_{AE}$ obeys pure attached-eddy scaling). Consequently, $\overline{u^2}_{\mathcal{L}}$ needs to be replaced by a component encompassing all remaining energy, denoted as $\overline{u^2}_G$, where subscript G stands for global. Wall-incoherent component $\overline{u^2}_{\mathcal{W}}$ remains unchanged, resulting in

$$\overline{u^2}^+ = \overline{u^2}^+_{\mathcal{W}} + \overline{u^2}^+_{AE} + \overline{u^2}^+_G. \tag{4.2}$$

For the data considered in figure 7, with $z_{\mathcal{L}} = 0.15\delta$, the three additive contributions of (4.2) are displayed in figure 11(*a–c*) and figure 11(*d–f*) for inner- and outer-scalings, respectively. The scaling of each component, in the logarithmic region, is now discussed.

The simplest approach for obtaining a scaling formulation for $\overline{u^2}_{\mathcal{W}}(z) = \int \phi^i_{\mathcal{W}}(z;\, k_x)\,\mathrm{d}k_x$ is to use Kolmogorov-type modelling, as used in previous works (see Spalart 1988; Marusic, Uddin & Perry 1997). Spectral scaling of $\phi^i_{\mathcal{W}}$ comprises a z-scaling at the low wavenumber end, while the higher wavenumber end adheres to a $k^{-5/3}$ scaling up to a wavenumber fixed in Kolmogorov scale η, see figures 15(*f*) and 21 in Part 1. When integrating a $k_x^{-5/3}$ model spectrum from $k_x z = c_1$ to $k_x z = c_2 z^{3/4}$, where c_1 and c_2 are constants, a scaling trend can be inferred. The latter boundary equals $k_x\eta = M$, with M being a constant and $\eta \equiv (\nu^3/\epsilon)^{1/4}$. From the $\epsilon \sim 1/z$ production–dissipation balance, we find that $k_x\eta = M \rightarrow k_x z = c_2 z^{3/4}$. Accordingly,

$$\overline{u^2}^+_{\mathcal{W}}(z) = \int_{k_x z = c_1}^{k_x z = c_2 z^{3/4}} \frac{K_0}{(k_x z)^{5/3}}\,\mathrm{d}(k_x z) = K_1 - \frac{K_2}{\sqrt{z}}, \tag{4.3}$$

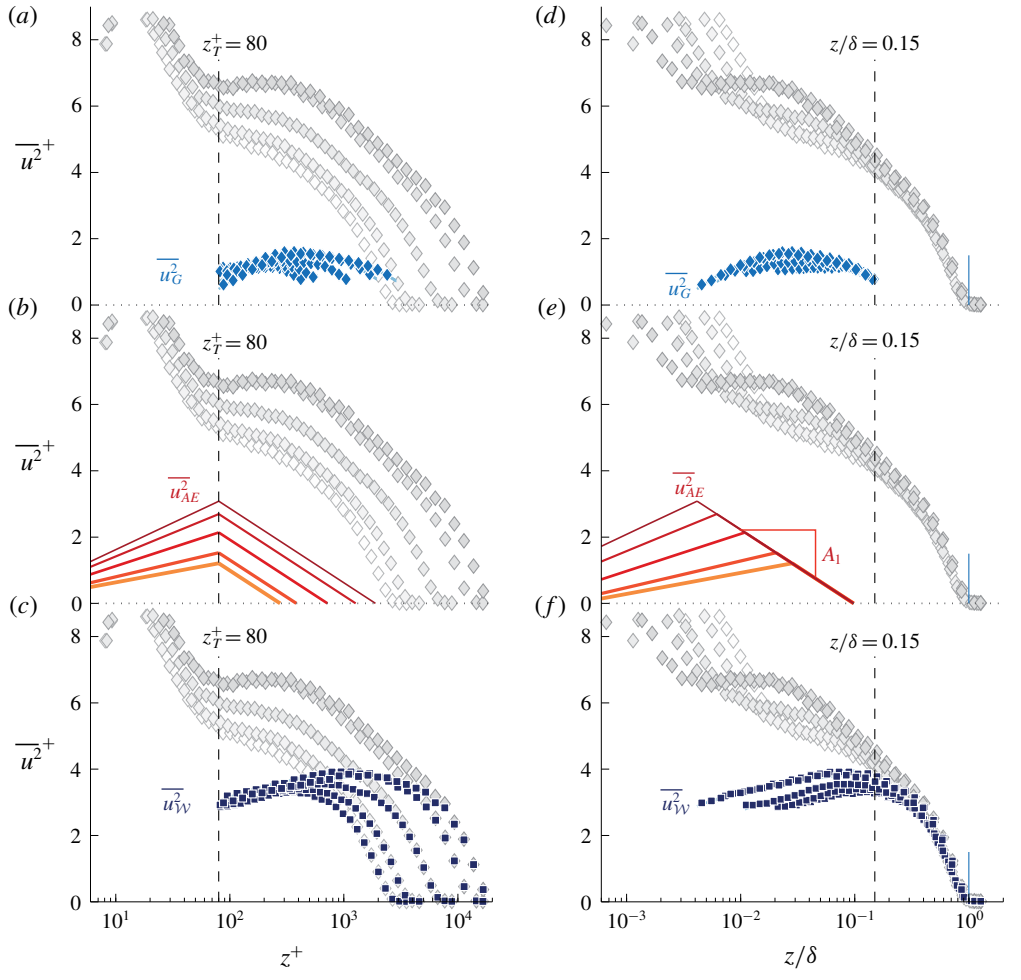

FIGURE 11. Streamwise TI profiles at a range of Reynolds numbers. Measured TI profiles are shown in each panel in light grey (duplicate from figure 6*a*). (*a–f*) In each of the three rows, TI profiles of one of the three sub-components are superposed. Inner-scaling and outer-scaling are used in (*a*,*c*,*e*) and (*b*,*d*,*f*), respectively.

where K_0, K_1 and K_2 are constants. When $Re_\tau \to \infty$, $\overline{u^2}^+_{\mathcal{W}}$ will tend towards K_1 for large z^+. At our practical values of Re_τ (figure 11*c*), $\overline{u^2}^+_{\mathcal{W}}$ is seen to increase up to $z \approx 0.10\delta$, after which a wake deviation occurs (Marusic *et al.* 1997). Fitting of (4.3) to the data in figure 11(*c*), for $z_T \leqslant z \leqslant 0.10\delta$, results largely in a Reynolds-number-invariant contribution, as shown by the profiles in figure 12(*a*); it was visually verified that (4.3) adequately described each experimental profile in figure 11(*c*). Experimental uncertainties in U_τ can be a cause for the slight variations observed in figure 12(*a*). Average values for the constants, from the five profiles, were found to be $K_1 = 4.01$ and $K_2 = 10.13$ (thick light blue line in figure 12*a*). By inspection, the data in figure 11(*c*) are not described by (4.3) above $z \approx 0.10\delta$. This deviation is expected since $\overline{u^2}^+_{\mathcal{W}}$ is strictly formed from the stochastic, wall-incoherent energy. At sufficiently large z, the wall-scaling of filter $f_{\mathcal{W}}$ breaks down and $\overline{u^2}^+_{\mathcal{W}}$

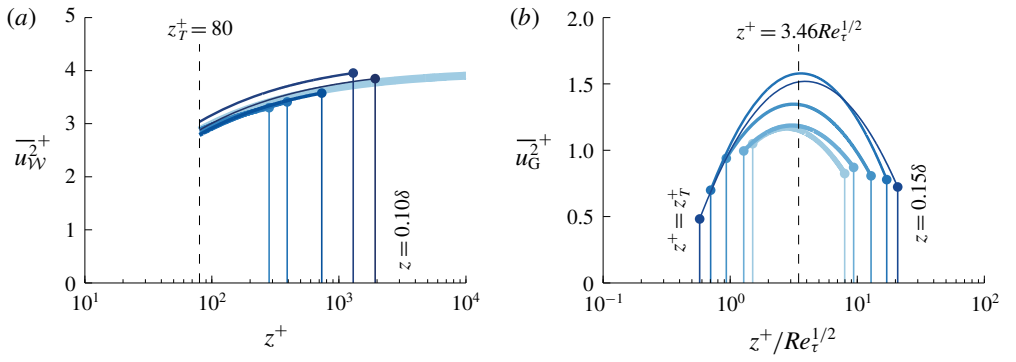

FIGURE 12. (*a*) Function fits via (4.3) to $\overline{u^2}_{\mathcal{W}}$ in figure 11(*c*) over the range $z_T \leqslant z \leqslant 0.10\delta$. The thick light blue line in the background presents (4.3) with the average values of $K_1 = 4.01$ and $K_2 = 10.13$. (*b*) Curve fits via (4.4) to $\overline{u^2}_G$ in figure 11(*a*) over the range $z_T \leqslant z \leqslant 0.15\delta$.

begins to include all turbulent scales (not just the scales from an inertial sub-range and dissipative end of the cascade). At the same time, the more limited scale separation in the wake, as well as the effects of intermittency on spectra (Kwon, Hutchins & Monty 2016), make it impossible to physically interpret the results in the wake region.

For the attached-eddy energy $\overline{u^2}_{AE}$, (2.5) was adopted. The near-wall decay trend following (3.3) is also drawn in figure 11(*b*,*e*). The vertical offset of the attached eddy (AE) component, being B_1 in (2.5), is dependent on the chosen $z_{\mathcal{L}}$. Further research should provide insight into what offset describes the stochastic statistics of attached structures (at what outer-scaled location $\overline{u^2}_{AE}$ should become zero). Conceivably, studies extracting instantaneous attached-eddy structures from full velocity fields can be instrumental to this (del Álamo *et al.* 2006; Lozano-Durán, Flores & Jiménez 2012; Hwang & Sung 2018; Solak & Laval 2018).

Finally, $\overline{u^2}_G$ appears as a broad hump throughout the logarithmic region (figure 11*a*,*d*) and was envisioned to be composed of mainly VLSMs/superstructures. No expressions exist for wall-normal profiles of the streamwise TI induced by such turbulence, despite the growing research interest in these types of large-scale turbulent motions by the wall-bounded turbulence community. Two decades ago, it was suggested that merging of self-similar large-scale motions (LSMs) may be one of the mechanisms generating VLSMs and superstructures (Adrian, Meinhart & Tomkins 2000). Only in recent studies however, it was concluded that wall-attached structures are related to an invariant solution of the Navier–Stokes equations and that those structures comprise families of self-sustaining motions that are consistent with self-similar, wall-attached eddy-scalings (Hwang, Willis & Cossu 2016; Cossu & Hwang 2017). Prior to that, a number of studies used linearized Navier–Stokes equations to show that long streaky motions can be amplified at all length scales (del Álamo *et al.* 2006; Hwang & Cossu 2010*a*,*b*, among others), and this is consistent with the recent findings that the large-scale outer structures involve self-sustaining mechanisms (de Giovanetti *et al.* 2017). Future studies remain necessary to reveal Reynolds-number scalings by way of resolving their spatial and temporal dynamics (Kerhervé, Roux & Mathis 2017) and by way of using promising techniques such as variational mode decompositions (Wang, Pan & Wang 2018). For now, a full

empirical formulation, judiciously chosen as a parabolic relation with logarithmic argument $\ln(z)$ via (4.4), was found to fit the data:

$$\overline{u^2}^+_G(z^+) = G_1 + G_2\ln(z^+) + G_3\ln(z^+)^2. \tag{4.4}$$

Figure 11(*b*) presents the five fits of (4.4), for $z_T \leqslant z \leqslant 0.15\delta$. Generally, its energy content increases with Re_τ, but a consistent monotonic trend is absent, owing to the experimental difficulties in acquiring repeatable and converged data at very large wavelengths (Samie 2017). Nevertheless, in light of our work, this component is responsible for the secondary peak (or hump) in $\overline{u^2}$ (Hultmark *et al.* 2012; Vallikivi *et al.* 2015; Willert *et al.* 2017; Samie *et al.* 2018). Marusic *et al.* (2013) observed that a lower bound of the logarithmic region resembled the $z^+ \propto Re_\tau^{1/2}$ dependence (Sreenivasan & Sahay 1997; Wei *et al.* 2005; Klewicki, Fife & Wei 2009; Morrill-Winter, Philip & Klewicki 2017), which is in agreement with the peak locations of $\overline{u^2}_G$ (see figure 12*b*). This explains that a steeper logarithmic decay – than one with $A_1 = 0.975$ – has been observed in raw, non-decomposed $\overline{u^2}$ profiles ($A_1 = 1.26$ in Marusic *et al.* 2013). Namely, we here suggest that this steeper decay beyond $z^+ \propto Re_\tau^{1/2}$ included a logarithmic energy decay of global/VLSM-type energy, superimposed on top of the attached-eddy decay. Interestingly, Hwang (2015) identified two self-similar families of structures, described as the LSMs and VLSMs, from channel flow simulations at relatively low Reynolds numbers up to $Re_\tau \approx 2000$. A self-similar structure of the VLSM content (alongside the self-similar structure of LSMs) supports our hypothesis of two dominant logarithmic decays (and recall that those will only be apparent at high Re_τ, when there is a sufficient wall-normal range for a logarithmic range of scales and when component $\overline{u^2}_{\mathcal{W}}(z)$ tends to a constant via (4.3) in the upper portion of the logarithmic layer).

5. Concluding remarks

A breakdown of the streamwise TI was assessed through the use of data-driven spectral filters for the streamwise velocity fluctuations u (derived and applied in Part 1). Within the logarithmic region, here taken from $z_T^+ = 80$ up to $z/\delta = 0.15$, the streamwise TI from three additive contributions is summarized in figure 13. The main outcomes of this work are listed as follows.

(i) Scaling trends of the TI reflecting wall-attached, self-similar eddying motions, revealed evidence for a logarithmic scaling following (2.5) with $A_1 = 0.975$ (constant over for the range of investigation: $2800 \lesssim Re_\tau \lesssim 19\,300$). A logarithmic decay via $\overline{u^2}_{AE} \propto A_1\ln(z/\delta)$ had to be assumed, because the wall-attached turbulence does comprise a signature of global/VLSM-type energy. It was hypothesized that this energy masks a true logarithmic region in the TI profiles, due to a bulge of $\overline{u^2}_G$ energy (figure 13*b*).

(ii) Constant $A_1 = 0.975$ is consistent with the growth of the near-wall TI, under the following assumptions: (I) the lower bound of the logarithmic region at which attached-eddy structures become influenced by viscosity scales in inner units (e.g. $z_T^+ = 80$); (II) below z_T^+ the energy footprint of wall-attached turbulence decays following (2.3); (III) the near-wall TI growth with Re_τ is solely caused by the footprint of the self-similar attached eddies. Assumption (III) implies that the very large-scale outer motions make a negligible contribution to the streamwise TI in the near-wall region (recall § 3), at least for the Re_τ range considered in

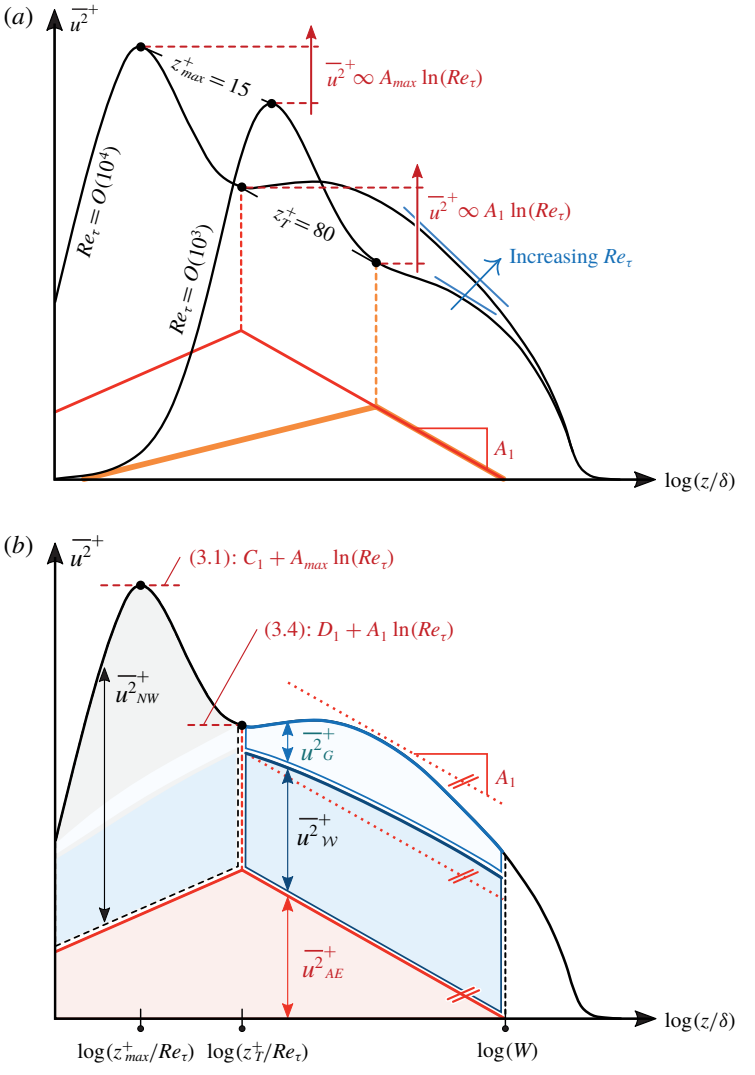

FIGURE 13. Decomposed structure of $\overline{u^2}(z)$ in ZPG turbulent boundary layers. (*a*) A low- and high-Reynolds-number turbulent boundary layer profile and (*b*) a breakdown of the streamwise turbulence intensity into three additive contributions in the logarithmic region ($z_T < z < W/\delta$), and two contributions in the near-wall region ($z < z_T$).

this study. When accepting these assumptions, the maximum in the near-wall TI profile at $z^+_{max} \approx 15$ disappears as a global maximum at $Re_\tau \approx 3.2 \times 10^7$ following a simple extrapolation (figure 10). Figure 13(*a*) illustrates the attached-eddy scaling in relation to the growth of the near-wall TI.

(iii) Two components other than the attached-eddy energy are present in the logarithmic region. The stochastically wall-incoherent energy scales following $\overline{u^2}^+_{\mathcal{W}}(z^+) = K_1 - K_2/\sqrt{z^+}$, with $K_1 = 4.01$ and $K_2 = 10.13$. This semi-empirical relation describes Kolmogorov turbulence residing at scales bounded by a z-scaled limit and a dissipation limit. When $Re_\tau \to \infty$, this energy asymptotes to $K_1 = 4.01$

at large z^+. A large-scale component $\overline{u^2}_G$ comprises global/VLSM-type energy. Other than that this energy seems weakly dependent on Re_τ (figure 12*b*), definite scaling trends cannot be provided and require future research.

Our current work may assist in the development of future data-driven models for the streamwise TI in ZPG TBL flow. Due to dissimilar scalings present over different ranges of the velocity energy spectra of the streamwise velocity u, an approach of considering individual sub-components of the streamwise TI, each having their spectral scaling, may be promising for new models. Our current work presented a breakdown of the streamwise TI in the logarithmic region into three components: a semi-empirical small-scale component comprising Kolmogorov-type turbulence, a model-based component following the AEH and a remaining contribution from non-self-similar global/VLSM-type energy. When in the near-wall region, the footprint of the self-similar attached-eddy contribution is superposed on a universal contribution $\overline{u^2}_{NW}$, the Reynolds-number growth of the near-wall TI can be related to an attached-eddy scaling.

Acknowledgements

We gratefully acknowledge the Australian Research Council for financial support and are appreciative of the publicly available DNS data of Sillero *et al.* (2013). We would also like to give special thanks to J. Monty, D. Krug, D. Chandran and H. Nagib for helpful discussions on the content of the manuscript.

REFERENCES

ABE, H., KAWAMURA, H. & CHOI, H. 2004 Very large-scale structures and their effects on the wall shear-stress fluctuations in a turbulent channel flow up to $Re_\tau = 640$. *Trans. ASME J. Fluids Engng* **126**, 835–843.

ADRIAN, R. J., MEINHART, C. D. & TOMKINS, C. D. 2000 Vortex organization in the outer region of the turbulent boundary layer. *J. Fluid Mech.* **422**, 1–54.

BAARS, W. J., HUTCHINS, N. & MARUSIC, I. 2016 Spectral stochastic estimation of high-Reynolds-number wall-bounded turbulence for a refined inner-outer interaction model. *Phys. Rev. Fluids* **1**, 054406.

BAARS, W. J., HUTCHINS, N. & MARUSIC, I. 2017*a* Reynolds number trend of hierarchies and scale interactions in turbulent boundary layers. *Phil. Trans. R. Soc.* A **375**, 20160077.

BAARS, W. J., HUTCHINS, N. & MARUSIC, I. 2017*b* Self-similarity of wall-attached turbulence in boundary layers. *J. Fluid Mech.* **823**, R2.

BAARS, W. J. & MARUSIC, I. 2020 Data-driven decomposition of the streamwise turbulence kinetic energy in boundary layers. Part 1. Energy spectra. *J. Fluid Mech.* **882**, A25.

BAIDYA, R., PHILIP, J., HUTCHINS, N., MONTY, J. P. & MARUSIC, I. 2017 Distance-from-the-wall scaling of turbulent motions in wall-bounded flows. *Phys. Fluids* **29**, 020712.

BULLOCK, K. J., COOPER, R. E. & ABERNATHY, F. H. 1978 Structural similarity in radial correlations and spectra of longitudinal velocity fluctuations in pipe flow. *J. Fluid Mech.* **88**, 585–608.

CHANDRAN, D., BAIDYA, R., MONTY, J. P. & MARUSIC, I. 2017 Two-dimensional energy spectra in a high Reynolds number turbulent boundary layer. *J. Fluid Mech.* **826**, R1.

CHEN, X., HUSSAIN, F. & SHE, Z.-S. 2018 Quantifying wall turbulence via a symmetry approach. Part 2. Reynolds stresses. *J. Fluid Mech.* **850**, 401–438.

CHO, M., HWANG, Y. & CHOI, H. 2018 Scale interactions and spectral energy transfer in turbulent channel flow. *J. Fluid Mech.* **854**, 474–504.

COSSU, C. & HWANG, Y. 2017 Self-sustaining processes at all scales in wall-bounded turbulent shear flows. *Phil. Trans. R. Soc.* A **375**, 20160088.

DAVIDSON, P. A. & KROGSTAD, P.-Å. 2009 A simple model for the streamwise fluctuations in the log-law region of a boundary layer. *Phys. Fluids* **21**, 055105.

DE GIOVANETTI, M., HWANG, Y. & CHOI, H. 2016 Skin-friction generation by attached eddies in turbulent channel flow. *J. Fluid Mech.* **808**, 511–538.

DE GIOVANETTI, M., SUNG, H. J. & HWANG, Y. 2017 Streak instability in turbulent channel flow: the seeding mechanism of large-scale motions. *J. Fluid Mech.* **832**, 483–513.

DEGRAAFF, D. B. & EATON, J. K. 2000 Reynolds number scaling of the flat-plate turbulent boundary layer. *J. Fluid Mech.* **422**, 319–346.

DEL ÁLAMO, J. C. & JIMÉNEZ, J. 2003 Spectra of the very large anisotropic scales in turbulent channels. *Phys. Fluids* **15** (6), L41–L44.

DEL ÁLAMO, J. C., JIMÉNEZ, J., ZANDONADE, P. & MOSER, R. D. 2006 Self-similar vortex clusters in the turbulent logarithmic region. *J. Fluid Mech.* **561**, 329–358.

HU, R. & ZHENG, X. 2018 Energy contributions by inner and outer motions in turbulent channel flows. *Phys. Rev. Fluids* **3**, 084607.

HULTMARK, M., VALLIKIVI, M., BAILEY, S. C. C. & SMITS, A. J. 2012 Turbulent pipe flow at extreme Reynolds numbers. *Phys. Rev. Lett.* **108** (9), 094501.

HUTCHINS, N., CHAUHAN, K., MARUSIC, I. & KLEWICKI, J. 2012 Towards reconciling the large-scale structure of turbulent boundary layers in the atmosphere and laboratory. *Boundary-Layer Meteorol.* **145**, 273–306.

HUTCHINS, N. & MARUSIC, I. 2007 Large-scale influences in near-wall turbulence. *Phil. Trans. R. Soc.* A **365**, 647–664.

HUTCHINS, N., NICKELS, T. B., MARUSIC, I. & CHONG, M. S. 2009 Hot-wire spatial resolution issues in wall-bounded turbulence. *J. Fluid Mech.* **635**, 103–136.

HWANG, J. & SUNG, H. J. 2018 Wall-attached structures of velocity fluctuations in a turbulent boundary layer. *J. Fluid Mech.* **856**, 958–983.

HWANG, Y. 2015 Statistical structure of self-sustaining attached eddies in turbulent channel flow. *J. Fluid Mech.* **767**, 254–289.

HWANG, Y. & COSSU, C. 2010*a* Amplification of coherent streaks in the turbulent Couette flow: an inputoutput analysis at low Reynolds number. *J. Fluid Mech.* **643**, 333–348.

HWANG, Y. & COSSU, C. 2010*b* Linear non-normal energy amplification of harmonic and stochastic forcing in the turbulent channel flow. *J. Fluid Mech.* **664**, 51–73.

HWANG, Y., WILLIS, A. P. & COSSU, C. 2016 Invariant solutions of minimal large-scale structures in turbulent channel flow for Re_τ up to 1000. *J. Fluid Mech.* **802**, R1.

KERHERVÉ, F., ROUX, S. & MATHIS, R. 2017 Combining time-resolved multi-point and spatially-resolved measurements for the recovering of very-large-scale motions in high Reynolds number turbulent boundar layer. *Exp. Therm. Fluid Sci.* **82**, 102–115.

KLEWICKI, J., FIFE, P. & WEI, T. 2009 On the logarithmic mean profile. *J. Fluid Mech.* **638**, 73–93.

KLEWICKI, J. C. 2010 Reynolds number dependence, scaling, and dynamics of turbulent boundary layers. *Trans. ASME J. Fluids Engng* **132**, 094001.

KLINE, S. J., REYNOLDS, W. C., SCHRAUB, F. A. & RUNDSTADLER, P. W. 1967 The structure of turbulent boundary layers. *J. Fluid Mech.* **30**, 741–773.

KWON, Y. S., HUTCHINS, N. & MONTY, J. P. 2016 On the use of the Reynolds decomposition in the intermittent region of turbulent boundary layers. *J. Fluid Mech.* **794**, 5–16.

LAVAL, J.-P., VASSILICOS, J. C., FOUCAUT, J.-M. & STANISLAS, M. 2017 Comparison of turbulence profiles in high-Reynolds-number turbulent boundary layers and validation of a predictive model. *J. Fluid Mech.* **814**, R2.

LEE, M. & MOSER, R. D. 2015 Direct numerical simulation of turbulent channel flow up to $Re_\tau = 5200$. *J. Fluid Mech.* **774**, 395–415.

LOZANO-DURÁN, A., FLORES, O. & JIMÉNEZ, J. 2012 The three-dimensional structure of momentum transfer in turbulent channels. *J. Fluid Mech.* **694**, 100–130.

MARUSIC, I., BAARS, W. J. & HUTCHINS, N. 2017 Scaling of the streamwise turbulence intensity in the context of inner-outer interactions in wall-turbulence. *Phys. Rev. Fluids* **2**, 100502.

MARUSIC, I., CHAUHAN, K. A., KULANDAIVELU, V. & HUTCHINS, N. 2015 Evolution of zero-pressure-gradient boundary layers from different tripping conditions. *J. Fluid Mech.* **783**, 379–411.

MARUSIC, I. & KUNKEL, G. J. 2003 Streamwise turbulence intensity formulation for flat-plate boundary layers. *Phys. Fluids* **15** (8), 2461–2464.

MARUSIC, I., MATHIS, R. & HUTCHINS, N. 2010*a* Predictive model for wall-bounded turbulent flow. *Science* **329** (5988), 193–196.

MARUSIC, I., MCKEON, B. J., MONKEWITZ, P. A., NAGIB, H. M., SMITS, A. J. & SREENIVASAN, K. R. 2010*b* Wall-bounded turbulent flows at high Reynolds numbers: recent advances and key issues. *Phys. Fluids* **22**, 065103.

MARUSIC, I. & MONTY, J. P. 2019 Attached eddy model of wall turbulence. *Annu. Rev. Fluid Mech.* **51**, 49–74.

MARUSIC, I., MONTY, J. P., HULTMARK, M. & SMITS, A. J. 2013 On the logarithmic region in wall turbulence. *J. Fluid Mech.* **716**, R3.

MARUSIC, I., UDDIN, A. K. M. & PERRY, A. E. 1997 Similarity law for the streamwise turbulence intensity in zero-pressure-gradient turbulent boundary layers. *Phys. Fluids* **9** (12), 3718–3726.

MATHIS, R., HUTCHINS, N. & MARUSIC, I. 2009 Large-scale amplitude modulation of the small-scale structures in turbulent boundary layers. *J. Fluid Mech.* **628**, 311–337.

MATHIS, R., HUTCHINS, N. & MARUSIC, I. 2011 A predictive inner–outer model for streamwise turbulence statistics in wall-bounded flows. *J. Fluid Mech.* **681**, 537–566.

METZGER, M. M., KLEWICKI, J. C., BRADSHAW, K. L. & SADR, R. 2001 Scaling the near-wall axial turbulent stress in the zero pressure gradient boundary layer. *Phys. Fluids* **13** (6), 1819–1821.

MONKEWITZ, P. A. & NAGIB, H. M. 2015 Large-Reynolds-number asymptotics of the streamwise normal stress in zero-pressure-gradient turbulent boundary layers. *J. Fluid Mech.* **783**, 474–503.

MONKEWITZ, P. A., NAGIB, H. M. & BOULANGER, W. 2017 Comparing the three possible scalings of stream-wise normal stress in turbulent boundary layers. In *10th International Symposium on Turbulence and Shear Flow Phenomena*.

MORRILL-WINTER, C., PHILIP, J. & KLEWICKI, J. 2017 An invariant representation of mean inertia: theoretical basis for a log law in turbulent boundary layers. *J. Fluid Mech.* **813**, 594–617.

MORRISON, J. F., JIANG, W., MCKEON, B. J. & SMITS, A. J. 2002 Reynolds number dependence of streamwise velocity spectra in turbulent pipe flow. *Phys. Rev. Lett.* **88** (21), 214501.

NICKELS, T. B., MARUSIC, I., HAFEZ, S. & CHONG, M. S. 2005 Evidence of the k_1^{-1} law in a high-Reynolds-number turbulent boundary layer. *Phys. Rev. Lett.* **95**, 074501.

ÖRLÜ, R., FIORINI, T., SEGALINI, A., BELLANI, G., TALAMELLI, A. & ALFREDSSON, P. H. 2017 Reynolds stress scaling in pipe flow turbulence—first results from CICLoPE. *Phil. Trans. R. Soc.* A **375**, 20160187.

PERRY, A. E. & ABELL, C. J. 1975 Scaling laws for pipe-flow turbulence. *J. Fluid Mech.* **67**, 257–271.

PERRY, A. E. & CHONG, M. S. 1982 On the mechanism of wall turbulence. *J. Fluid Mech.* **119**, 173–217.

PERRY, A. E., HENBEST, S. & CHONG, M. S. 1986 A theoretical and experimental study of wall turbulence. *J. Fluid Mech.* **165**, 163–199.

PERRY, A. E. & LI, J. D. 1990 Experimental support for the attached-eddy hypothesis in zero-pressure-gradient turbulent boundary layers. *J. Fluid Mech.* **218**, 405–438.

ROSENBERG, B. J., HULTMARK, M., VALLIKIVI, M., BAILEY, S. C. C. & SMITS, A. J. 2013 Turbulence spectra in smooth- and rough-wall pipe flow at extreme Reynolds numbers. *J. Fluid Mech.* **731**, 46–63.

SAMIE, M. 2017 Sub-miniature hot-wire anemometry for high Reynolds number turbulent flows. PhD thesis, The University of Melbourne, Melbourne, Australia.

SAMIE, M., MARUSIC, I., HUTCHINS, N., FU, M. K., FAN, Y., HULTMARK, M. & SMITS, A. J. 2018 Fully-resolved measurements of turbulent boundary layer flows up to $Re_\tau = 20000$. *J. Fluid Mech.* **851**, 391–415.

SILLERO, J. A., JIMÉNEZ, J. & MOSER, R. D. 2013 One-point statistics for turbulent wall-bounded flows at Reynolds numbers up to $\delta^+ \approx 2000$. *Phys. Fluids* **25**, 105102.

SMITS, A. J., MCKEON, B. J. & MARUSIC, I. 2011 High Reynolds number wall turbulence. *Annu. Rev. Fluid Mech.* **43**, 353–375.

SOLAK, I. & LAVAL, J.-P. 2018 Large-scale motions from a direct numerical simulation of a turbulent boundary layer. *Phys. Rev.* E **98**, 033101.

SPALART, P. R. 1988 Direct simulation of a turbulent boundary layer up to $Re_\theta = 1410$. *J. Fluid Mech.* **187**, 61–98.

SREENIVASAN, K. R. & SAHAY, A. 1997 The persistence of viscous effects in the overlap region and the mean velocity in turbulent pipe and channel flows. In *Self-Sustaining Mechanisms of Wall Turbulence* (ed. R. Panton), pp. 253–272. Computational Mechanics Publications.

TOWNSEND, A. A. 1976 *The Structure of Turbulent Shear Flow*. Cambridge University Press.

VALLIKIVI, M., GANAPATHISUBRAMANI, B. & SMITS, A. J. 2015 Spectral scaling in boundary layers and pipes at very high Reynolds numbers. *J. Fluid Mech.* **771**, 303–326.

VASSILICOS, J. C., LAVAL, J.-P., FOUCAUT, J.-M. & STANISLAS, M. 2015 The streamwise turbulence intensity in the intermediate layer of turbulent pipe flow. *J. Fluid Mech.* **774**, 324–341.

VINCENTI, P., KLEWICKI, J. C., MORRILL-WINTER, C., WHITE, C. M. & WOSNIK, M. 2013 Streamwise velocity statistics in turbulent boundary layers that spatially develop to high Reynolds number. *Exp. Fluids* **54** (12), 1–13.

WANG, W., PAN, C. & WANG, J. 2018 Quasi-bivariate variational mode decomposition as a tool of scale analysis in wall-bounded turbulence. *Exp. Fluids* **59** (1), 1–18.

WEI, T., FIFE, P., KLEWICKI, J. C. & MCMURTRY, P. 2005 Properties of the mean momentum balance in turbulent boundary layer, pipe and channel flows. *J. Fluid Mech.* **522**, 303–327.

WILLERT, C. E., SORIA, J., STANISLAS, M., KLINNER, J., AMILI, O., EISFELDER, M., CUVIER, C., BELLANI, G., FIORINI, T. & TALAMELLI, A. 2017 Near-wall statistics of a turbulent pipe flow at shear Reynolds numbers up to 40 000. *J. Fluid Mech.* **826**, R5.

WINKEL, E. S., CUTBIRTH, J. M., CECCIO, S. L., PERLIN, M. & DOWLING, D. R. 2012 Turbulence profiles from a smooth flat-plate turbulent boundary layer at high Reynolds number. *Exp. Therm. Fluid Sci.* **40**, 140–149.

YAMAMOTO, Y. & TSUJI, Y. 2018 Numerical evidence of logarithmic regions in channel flow at $Re_\tau = 8000$. *Phys. Rev. Fluids* **3**, 012602.